Delft University of Technology

Electro Facies Based Lithology and Mechanical Modeling

A Proposed Workflow and Models Linkage

Abdulmohsen Al-Mansour

TU Delft Delft University of Technology

Electro Facies Based Lithology and Mechanical Modeling

A Proposed Workflow and Models Linkage

By

Abdulmohsen Al-Mansour

in partial fulfillment of the requirements for the degree of

Master of Science
in Petroleum Engineering and Geoscience

at the Delft University of Technology,
to be defended publicly on Monday August 27, 2016 at 13:45

Supervisor:	Assist. Prof. Dr. A. Barnhoorn	TU Delft
Co-Supervisor:	Dr. N. Filippidou	Shell
Thesis committee:	Prof. Dr. P.L.J. Zitha	TU Delft
	Dr. Ir. D.S. Draganov	TU Delft

TU Delft Delft University of Technology

Abstract

The induced seismic activities and subsidence in the Groningen region urges for deeper investigation of the mechanical elastic parameters and lithological facies. A recently (2015) drilled well in the area of Zeerijp has provided a rich dataset from the Permian and Carboniferous to be analyzed and eventually help to understand and characterize the penetrated intervals.

The well was cored and logged extensively, providing a wide and diverse database that includes well logs, computed tomography (CT) scans, x-ray diffraction (XRD), petrography, routine core analysis (RCAL), scratch test, unconfined compression test (UCS) and triaxial compression test (TCS). These data were integrated using the disciplines of petrophysics, rock physics, geology and geomechanics, in order to analyze and build one lithology- and one mechanical- data based model that describe the Permian and Carboniferous section.

Each lithology- and mechanical- model consisted of six different facies; four sandstones and two shales facies were classified using the data and the understanding of the geological depositional model. The generated geology-reflected lithology facies model with the proposed workflow can aid into building a more reliable 3D geological model. The benefits of this methodology can be extended to assist in a more robust dynamic modeling. Additionally, the mechanical model can be used to provide granularity in previous mechanical models, not only for the reservoir, but also for the over- and under-burden. The two models (lithology- and mechanical-facies model) correlate 70% in general.

Acknowledgement

This work wouldn't have been possibly done without the help and guidance from Aletta Filippidou. With great gratitude, I grant her the first thanks and appreciation. Her endless help, providing logistics, input, guidance, supervision and follow up through every stage of the project. I had the honor to work under my TU Delft advisor Auke Barnoorn. His support, inputs and guidance were remarkable and added an extra value to the study. I also thank NAM for giving me the opportunity and have their trust bestowed on me to analyze the data and make it available to the public domain. Thanks to Shell's generosity for creating the comfortable environment by providing the resources such as laptop, license, office and support. On the individual level, a special thanks to Jan Van Elk and Dirk Doornhof from NAM for their comments, guidance and support. I also thank Arjan van der Linden, Fons Marcelis, Sander Hol and Hong Xian from Shell for their inputs and guidance on this work.

Contents

1. Introduction

As hydrocarbon reservoirs consume their depletion drive potential during production, pore pressure drops, allowing other stresses to play a role in the reservoir's geomechanics. As a result, and if the pressure drop is sufficient, pore pressure fails to act against grain pressure, and compaction may take place. Many surface subsidence examples around the world from reservoir compaction can be mentioned, for example Ekofisk and Wilmington fields (Allen & Mayugai, 1969) (Sulak, 1991).

The compaction effect in the subsurface can appear on the surface in the form of land subsidence and seismic activities (Thienen-Visser & Peter A., 2017) (Van Thienen-Visser, et al., 2015). Since 1986, several seismic activities with a magnitude ranging from -0.8 to 3.6 has taken place in a various gas fields in the Netherlands (Van Thienen-Visser, et al., 2015). Land subsidence measurements recorded a maximum of 33 cm in the subsidence bowl (Anon., n.d.). This phenomenon can cause major issues in many aspects such as well casing, infrastructure and land structures.

Figure 1. Location map of the Groningen field.

The Groningen field is located in the northeastern part of the Netherlands (Figure 1). An exploration well in 1959 showed a gas discovery in the clastic Permian Rotliegend formation. Production started four years later (Thienen-Visser & Peter A., 2017). The field is estimated to withhold almost 2.925 trillion cubic meters of gas initially in place (2.925 TCM or ~100 TCF).

In 1991, seismic events started to appear in the northern part of the field area, where it used to be considered seismically inactive. Event density and intensity took an increasing trend throughout the field life with a hypocenter depth that matches the reservoir depth. Many studies performed, for example by

TNO (TNO, 2013), have showed a relation between compaction and pressure changes, due to depletion, in the reservoir. Ever since the discovery of the field until 2015, the cumulative production of gas sums to about 75% of the initial reserves estimation (2.115 TCM) (Breunese & Theinen-Visser, 2015) over a pressure decline from 347 bar (virgin) to 95 bars as of 2016. On the 28th of March 2018, following a 3.4R magnitude earthquake in January 2018, the Dutch Prime Minister Mark Rutte announced a decision, by the parliament, for Groningen field to stop producing by 2030 (Fleming, 2018) (Meliksetian, 2018).

Seismicity and compaction have been related to gas production and associated pressure depletion. Compressibility is defined as a measure of the relationship between volume change and the exerted pressure of a body (Zimmerman, 1990). To notice reservoir compaction at the surface, few conditions need to be met regarding the reservoir formation. These conditions are: significant reservoir pressure drop, highly compressible reservoir rock (soft), considerable thickness and significant compaction occurrence (not shielded by overburden) (Fjaer, et al., 2008).

Therefore, and in an attempt to model and understand rock mechanical properties and responses, ZRP-3A well was drilled and logged with gamma ray, neutron, density, resistivity, image log and acoustic tools for a total of 370m, covering the overburden formation (Ten Boer), the reservoir and the underburden (Carboniferous). The well was extensively cored and approximately 200m of core was retrieved. From the core, several core samples were extracted. Routine Core Analysis (RCAL), Special Core Analysis (SCAL), petrography and mechanical experiments were conducted on the core by several research partners.

2. Problem statement

With the abundance of basic logging operations, lithology can be easily identified and characterized and three-dimensionally modeled with confidence, ultimately to be confirmed using direct core observations. On the other hand, coring operations are limited due to its cost. Additionally, core preparation and execution specifically of mechanical experiments and studies is resource intensive and time consuming. Therefore, building a three-dimensional (3D) geomechanical model based on lab experiments with an acceptable confidence is challenging, costly and time consuming. Moreover, although (log-based) electrofacies modeling is widely and routinely performed in the Oil&Gas industry as input to 3D static models, integrating discrete and continuous mechanical measurements directly from the core is not commonly practiced, hence creating a “mechanical” electrofacies model.

Static or dynamic elastic properties are difficult to predict accurately from well logs because mechanical parameters depend on variables that are not directly measured by basic well logging tools, such as pore shape, size and accurate mineral composition. Thus, log produced dynamic mechanical parameters need to be calibrated with the elastic measurement from lab experiments.

Gas production results in pore pressure reduction in the reservoir. With a significant pressure drop, consequently, forces change, which eventually may lead to compaction. Lithological facies can act differently in hydrocarbon sweep, similarly, mechanical facies can also act differently in the elastic zone.

Dynamic elastic mechanical parameters and lithology can be estimated using well logging measurements. However, before performing such estimation, the logging conditions need to be accounted for. The pore’s filling fluid composition and stress conditions, in addition to borehole condition, influence log measurements. Overlooking these parameters can mislead and bias the interpretation.

Compaction in the Groningen urges to find a way to model the reservoir geomechanically to understand its reaction while continuing to produce and deplete. As there are about only 12 years left of production with continuous reduction in gas amounts each year, it is important to understand the mechanical properties and field responses to optimize the plan for gas production while ensuring a safe environment on the surface during the process.

3. Study goal

The objective of this study is to propose a mechanical facies model as well as the workflow that builds it. The method proposes a geomechanical facies models using wireline log-derived and mechanical properties relevant information. Later, the mechanical electrofacies model is compared against a conventionally built electrofacies/lithological model. The models testing and comparison provides an insight about where the two models are matching and where they differ.

The workflow also aims to discuss the different data scales used; from the continuous electrical logs and the continuous and spot lab measurements to provide an input parameters and variables for the mechanical and lithological static modeling.

The proposed workflow is the following:

- Log preparation (editing, depth matching and reconstruction).
- Log modelling to achieve complete depth coverage.
- Routine core analysis preparation (with depth matching to logs)..
- Continuous core measurements preparation (resolution matching, depth shifting)
- Data interpretation through saturation, porosity and fluid substitution.
- Log data calibration to core through log porosity to core porosity, density proxy from computed tomography (CT) scans etc.
- Build electro-lithological facies model using clay volume and total porosity logs.
- Build electro-mechanical facies model using Young's modulus, Bulk modulus and quasi-unconfined compressive strength (UCS) scratch log.

4. Literature review

First attempts to model compaction were accomplished by McCann and Wilts in 1951 to understand the compaction in Wilmington field (McCann & Wilts, 1951). In 1973, Geertsma highlighted the compaction hazard and attempted to model compaction in the Groningen field (Geertsma, 1973). Later, more studies were performed by others using theoretical approaches (Segall, 1992) (Van Opstal, 1974) (Wang, et al., 2006)(Hejmanowski, 1995). However, these studies assume homogenous reservoir of the large Groningen field (Thienen-Visser & Peter A., 2017).

Since 1973, many studies have been using different approaches to help approximate mechanical responses by applying theoretical approaches (Thienen-Visser & Peter A., 2017). Nucleus of strain theory was used by Greetsma to estimate subsidence and how it is distributed using pressure depletion (Geertsma, 1973). However, Geertsma's method assumes homogenous reservoir, with land subsidence and pressure drop as inputs, to estimate compressibility using volume strain. Also, the method assumes linear elastic property. Many others have adopted nucleus of strain theory as an influence tool method

(Segall, 1992) (Van Opstal, 1974) (Wang, et al., 2006). Also, stochastic theory was used to estimate compaction (Hejmanowski, 1995).

Most recent studies are using time decay, isotach and rate type compaction models (NAM, 2013) (Den Haan, 1994) (TNO, 2013). The time decay model uses a time factor to delay the response of subsidence while pressure is depleted. The other models are instantaneous. Rate type compaction, conducted by NAM, has incorporated lab measurements of a compressibility factor and related it with porosity exponentially. However, they reported that their compressibility-porosity model has a high uncertainty window with compressibility having a fold factor of 5. Rate type compaction model has been used with different approaches, forward modeling and inversion modeling (TNO, 2013) (Thienen-Visser & Peter A., 2017). Both approaches reported mismatches between the model output and the real values and rooted the cause to the porosity estimation inaccuracy in the geological model and aquifer activity (Van Thienen-Visser, et al., 2015).

Model correlation between lithology and mechanical facies model is rarely practiced or witnessed. Yale & Jamieson (1994) used a predefined lithological facies model from core with XRD data then performed dynamic and static elastic properties correlation.

5. Geological background of the section

The Rotliegend Formation is divided into two members, Slochteren and Ten Boer (Figure 2). The Slochteren member has a wide variety of colors, grain sizes and grain sortness. Lower Slochteren mainly represents the wadi deposits, conglomerates, sand and clay layers. Upper Slochteren represents dune facies. Ten Boer member is interpreted as sabkha deposits. It mainly consists of silt, clay and fine sand with anhydrite nodules (Stauble & Milius, 1970).

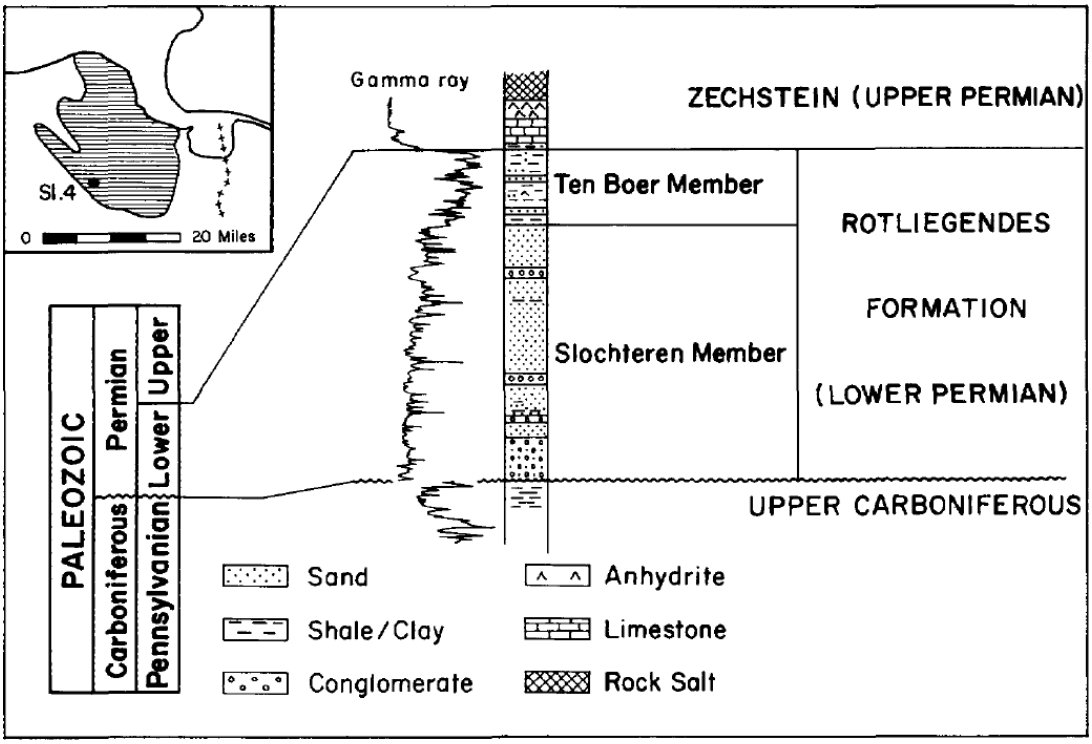

Figure 2. Stratigraphy, from well Sl.4, of the Lower Permian in Groningen Field (Stauble & Milius, 1970).

The logged study section exposes the Carboniferous and lower Permian age lithologies (Figure 3). During the Carboniferous, the igneous Variscan orogeny has been the source of sediments to deposit a deltaic shale, sandstone and coal facies that make the Carboniferous shale section. Later, volcanic activities and non-deposition events created an unconformity to mark the contact between Carboniferous and Permian times. Lower Permian witnessed the deposition of Rotliegend formation (Stauble & Milius, 1970). The depositional environments were interpreted to be an alluvial, wadi and aeolian with dune, sand flats and playa lakes under arid and semi-arid climate conditions (Gaupp & Okkerman, 2012).

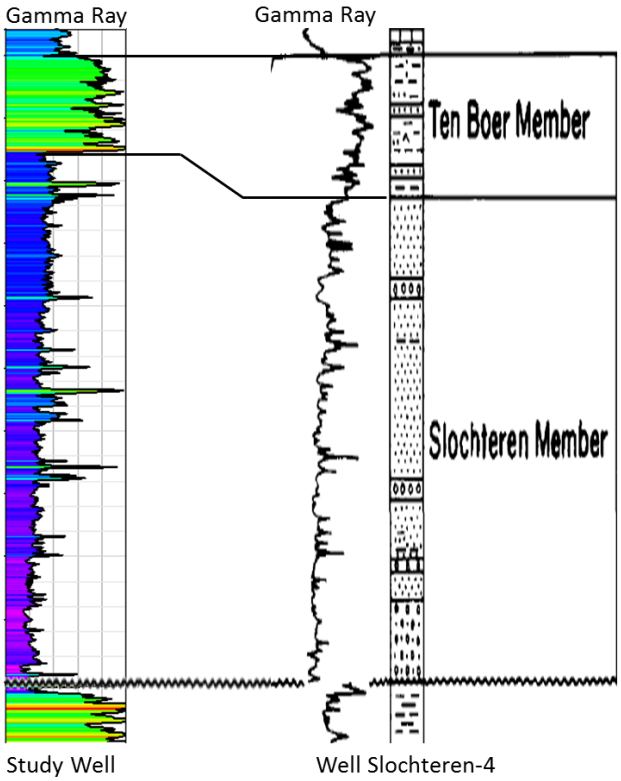

Figure 3. Correlation, using Gamma Ray, between the study well and well Slochteren-4 from (Stauble & Milius, 1970).

Diagenetic events have a major role in the reservoir properties. Many diagenetic processes took place leaving a wide variety of authigenic minerals; early, burial-related, temperature-related etc. diageneses processes have caused many minerals to form such as clays, metal oxides, carbonates, evaporites and quartz (Gaupp & Okkerman, 2012). In arid conditions, these minerals precipitate out as they run down to water table due to water evaporation and the resultant increasing salinity (Wright, 1992) (Figure 4).

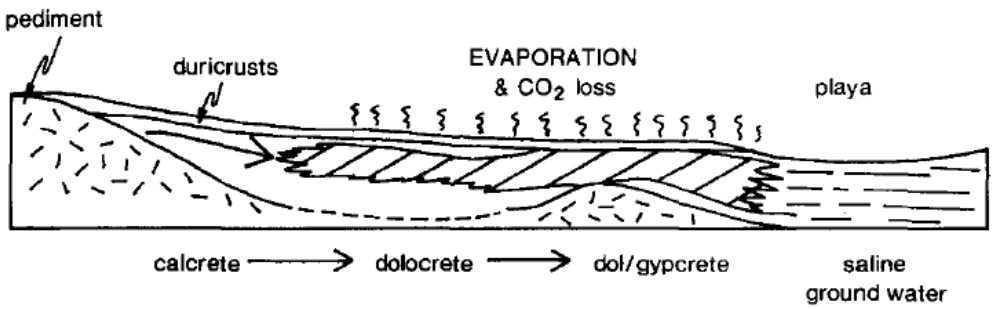

Figure 4. Water movement in an arid environment and its mineral precipitation profile from (Wright, 1992).

6. The Dataset:

6.1. Electrical Well Logs Data

The study section has been logged with Schlumberger® wireline tools under open hole condition. The logging operation included gamma ray, neutron porosity, density, acoustic and resistivity tools. Data shows spiking or disturbance at the very top. This can be possibly due to the casing collar. Acoustic data in the lower part of the carboniferous section show constant and unrealistic measurements. Shear and compressional slowness recorded 51 and 36 µs/ft respectively. Borehole temperature was recorded across the section with an average value of 114°C. Figure 5 shows the acquired wireline and the interpreted data.

6.2. Interpreted Logs

The following logs were provided by the asset team in NAM. They were interpreted using the open hole logs mentioned in section 6.1.

6.2.1. Cation Concentration Volume (Qv)

Cation concentration volume (Qv) (Figure 5) parameter is the cation exchange capacity (CEC) per unit of pore volume for clays. It is used to account for the extra conductivity of clays in shaley sands when using the Waxman-Smith equation to calculate water saturation. (McPhee, et al., 2015).

6.2.2. Water Resistivity (Rw)

Water resistivity (Figure 5) is an important parameter to perform calculation such as water saturation or estimate brine density and to acquire brine information. Overall, water resistivity seems almost constant across the reservoir section with an average value 0.0116 Ω.

6.2.3. Clay volume

The interpreted clay volume log was only confined to the sand section. Clay volume can be estimated from gamma ray log through equation 1.

$$Clay\ Volume = \frac{GR_{clay} - GR_{log}}{GR_{clay} - GR_{sand}} \quad (1)$$

GR_{clay}= Gamma ray reading in clay (API)

GR_{sand}= Gamma ray reading in clean sand (API)

GR_{log}= Gamma ray reading from log(API)

6.2.4. Total Porosity

Total porosity was interpreted using the density-neutron method, θ_{ND} (Equation 3). This is a common method (Equation 3) (Gaymard & Poupon, 1968) to perform total porosity calculation in gas bearing sand reservoirs (Ijasan, et al., 2013). This method uses both neutron porosity values from the neutron porosity log, Φ_N, and density porosity, Φ_D (Equation 2). The porosity log, interpreted and provided by the asset team, was only interpreted for the sandstone section (Figure 5).

$$\emptyset_D = \frac{\rho_m - \rho_{log}}{\rho_m - \rho_f} \tag{2}$$

$$\emptyset_{ND} = \sqrt[2]{\frac{\emptyset_D{}^2 + \emptyset_N{}^2}{2}} \tag{3}$$

ρ_m = matrix density (g/cc)
ρ_{log} = log density (g/cc)
ρ_f = fluid density (g/cc)

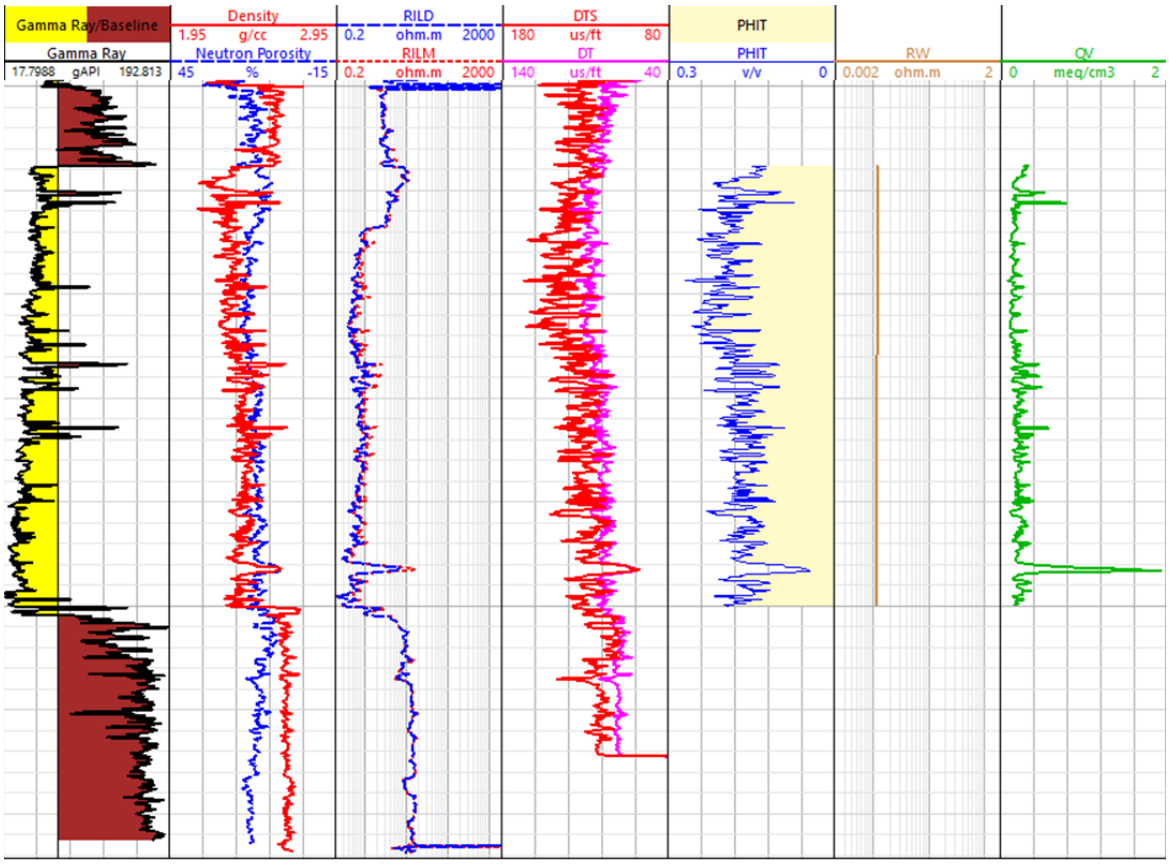

Figure 5. Log view of the acquired wireline data of Well ZRP-3A. From left to right, track 1 is showing gamma ray with baseline at 75 API. Track 2 is showing neutron porosity and density. Track 3 is showing deep (RILD) and medium (RILM) resistivity. Track 4 is showing shear (DTS) and compressional (DTC) slowness. Track 5, 6 and 7 show an interpretation, from asset team, of total porosity (PHIT), formation water resistivity (RW) log and cation concentration volume (QV).

6.3. Core Data

Eight core sections were retrieved from the well. Cores 1 to 6 are continuous covering Ten Boer and Upper Slochteren. Cores 7 and 8 were cut in the Carboniferous shales of the underburden. Core lengths vary between 17 and 30 meters. Many vertical and horizontal plugs were extracted for various test experiments. At the time of writing, most of the analysis was limited on the cores 1 to 6.

6.3.1. Routine Core Analysis (RCAL)

Several vertical plugs have been extracted from core and sent to different labs, including Shell, ExxonMobil and Utrecht University, for routine core analysis and other tests. Plugs that have been analyzed in Shell were tested for porosity, permeability and grain density (Appendix 1a). The tests were performed at ambient conditions. Plug analysis performed by ExxonMobil included porosity measurements at reservoir conditions (stressed) for some plugs. (Appendix 1b).

Core porosity estimation done by Shell was performed by measuring bulk volume (V_b) and grain volume (V_g) (Equation 4). Bulk volume was measured using two methods, mercury buoyancy and caliper. Grain volume was measured using Chloroform (CCl_3H). Quantifying porosity using mercury buoyancy is more reliable than using caliper, as highlighted by the lab spreadsheet report. However, most of the samples were not measured with mercury. Therefore, caliper-measured bulk volume was used to quantify porosity. Figure 6 shows a log view of the RCAL test measurements.

$$\emptyset = \frac{V_g}{V_b} \tag{4}$$

RCAL tests conducted by ExxonMobil (XOM) has also included total porosity. Samples were oven-dried to 110-115°C. The porosity measurements from XOM labs included stressed and unstressed porosity at 3300 psi (22.75 MPa) and 500-800 psi (3.45-5.52 MPa) respectively.

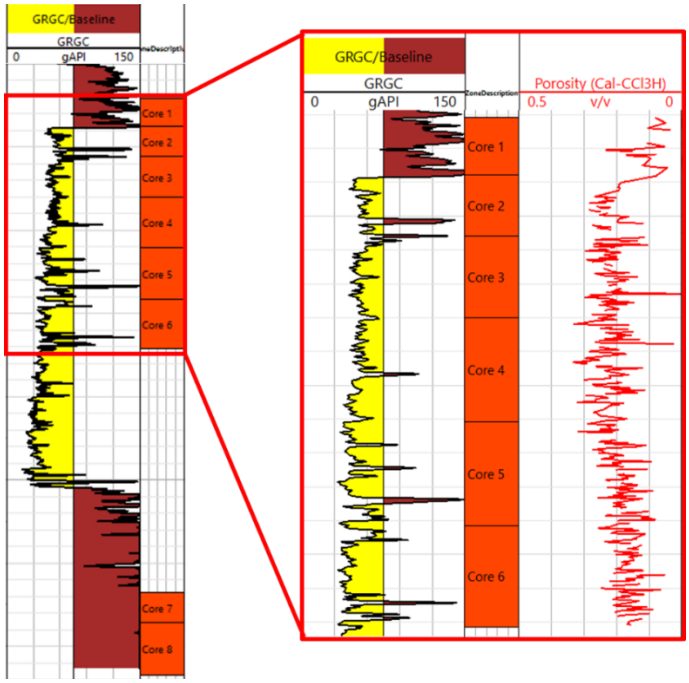

Figure 6. Log view of the porosity measurements from Routine Core Analysis.

6.3.2. Petrography

Petrography was performed on twenty-five samples by an external lab (PanTerra). The sample selection is spread across the upper part of the Slochteren sandstone section. A detailed thin section description and mineral identification has been made. Figure 7 shows the samples locations. The petrography analysis can be found in Appendix 2.

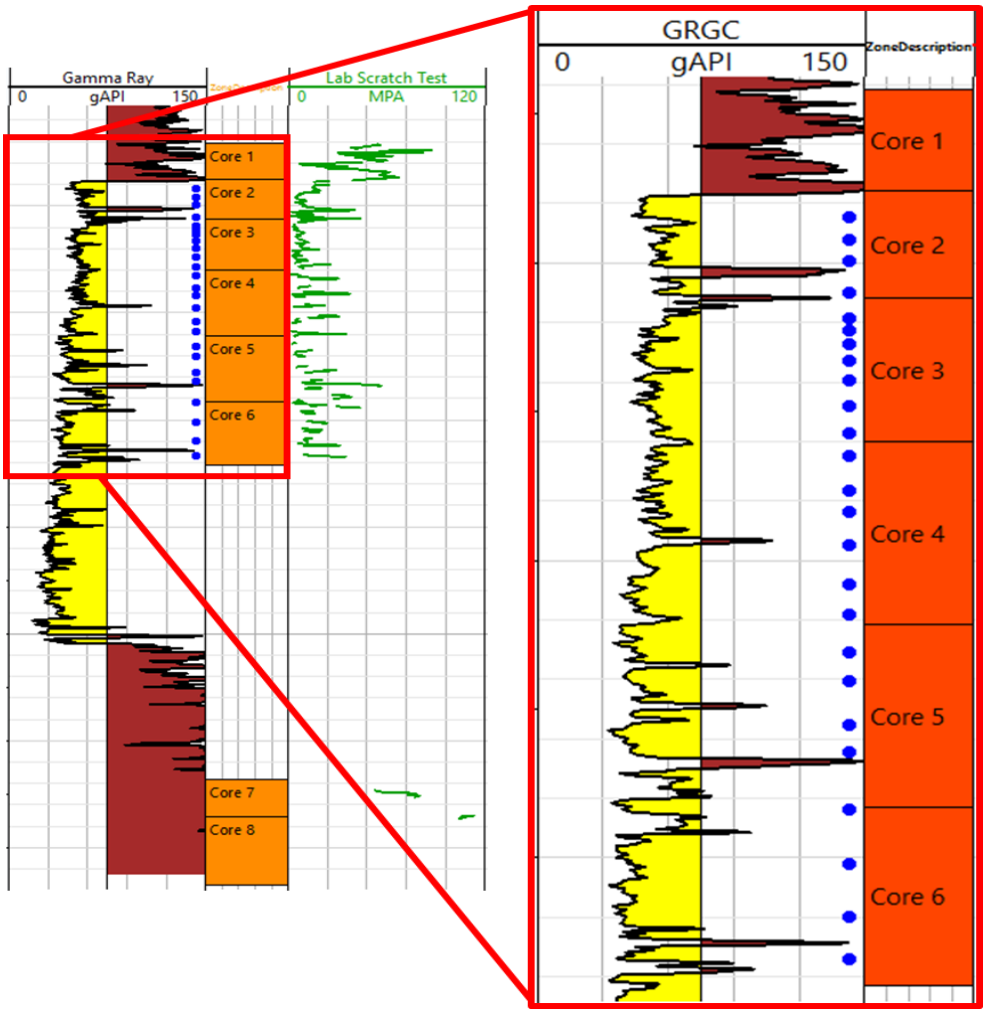

Figure 7. Log view of the samples locations that were selected for petrography (blue dots), depth-wise, in the gamma ray log track (GRGC) with baseline at 75 API to qualitatively differentiate sand (yellow) and shale (brown) visually. Also, values from scratch test.

6.3.3. Laser Particle Size Analysis (LPSA)

Laser Particle Size Analysis method uses laser light scattering to estimates grain volume by measuring a single diameter of the grain. The measured diameter is converted to an equivalent diameter of sphere (Ballard & Beare, 2016). Twenty-three plug samples were tested with GRADISTAT computer program for LPSA (Appendix 3). The data were inherited from Hol, et al. (2018). Mean, skewness, kurtosis and sorting analysis of the grains were calculated using geometric method of moment (Equation 5, 6, 7 and 8) (Simon & Pye, 2001). Different variety of grain sizes were covered in this analysis. Very fine sand size (140 µm) to very coarse sand size (~1000 µm) were measured. Skewness, sorting and kurtosis varied between -1.6 to -2.7, 3 to 7.2 and 6.9 to 11.6, respectively.

$$mean = \tilde{x} = e^{\frac{\sum f \ ln \ m_m}{100}} \quad (5)$$

$$Standard\ deviation\ (sorting) = \sigma = e^{\sqrt{\frac{\sum f\ (ln\ m_m - \ln \tilde{x})^2}{100}}} \quad (6)$$

$$Skewness = \frac{\sum f\ (ln\ m_m - \ln \tilde{x})^3}{100 \ln \sigma^3} \quad (7)$$

$$Kurtosis = \frac{\sum f\ (ln\ m_m - \ln \tilde{x})^4}{100 \ln \sigma^4} \quad (8)$$

Description of sorting, skewness and kurtosis as mentioned in Simon & Pye (2001):

Sorting		Skewness		Kurtosis	
Very well sorted	<1.27	Very fine skewed	<-1.30	Very platykurtic	<1.70
Well sorted	1.27-1.41	Fine skewed	-1.30 to -0.43	Platykurtic	1.70-2.55
Moderately well sorted	1.41-1.62	Symmetrical	-0.43 to +0.43	Mesokurtic	2.55-3.70
Moderately sorted	1.62-2	Coarse skewed	+0.43 to +1.30	Leptokurtic	3.70-7.40
Poorly sorted	2-4	Very coarse skewed	>+1.30	Very leptokurtic	>7.4
Very poorly sorted	4-16				
Extremely poorly sorted	>16				

6.3.4. Scratch test

The scratch test method was developed during late 90's by the University of Minnesota. Epslog's Wombat™ rock strength device was used to conduct the scratch experiment (Figure 8) and produce the data. This method is almost non-destructive, fast, robust, provides one-to-one relation with UCS and can provide a high resolution of 0.5 cm scale with high accuracy of about 1 N (Ferreira, et al., 2016) to enable for fine-scale heterogeneity investigation if needed (Richard, et al., 2012) (Germay, et al., 2015).

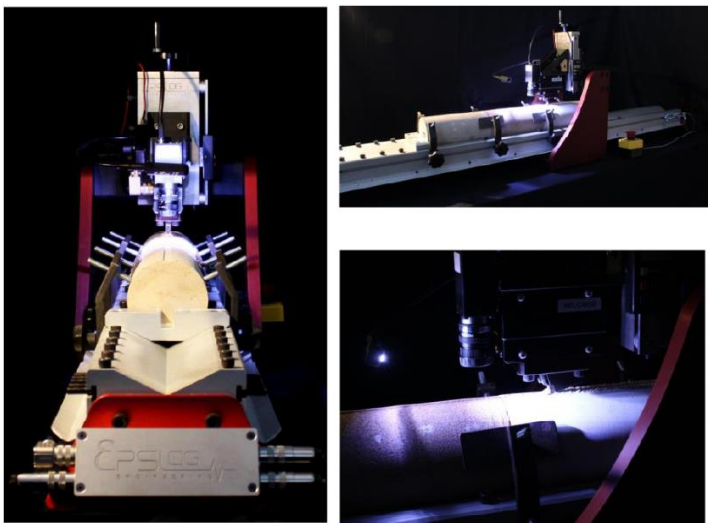

Figure 8. Wombat™ rock strength device from Epslog.

The experiment is conducted by laying down the core in the device then apply a force with a 1 cm wide cutter on the core. As the force is applied, a few millimeters groove mark is caused. The force applied versus the groove cross sectional area, the groove width multiplied by the groove depth, can plotted on a linear curve that its slope is considered as the intrinsic specific energy (ISE), or ε (Figure 9). ISE is proportional to UCS (Ferreira, et al., 2016) (Figure 10). The experiment time is very fast relative to conventional procedure for UCS determination. The operation doesn't require sample preparation and can analyze 20 m per day. Also, this method provides a continuous log rather than sample plug point values. In this work, the resulted log from the scratch test is used as a (continuous) proxy to (discrete) unconfined stress tests.

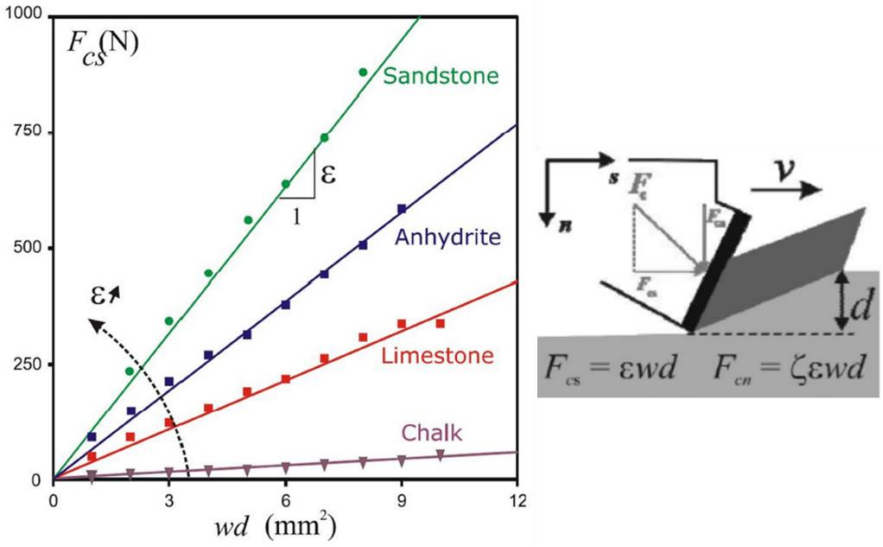

Figure 9. (Left) Wombat™ standard ISE profiles for different lithologies (Right) Schematic diagram of the cutter and surface with the forces acting on it (Dagrain & Germay, 2006).

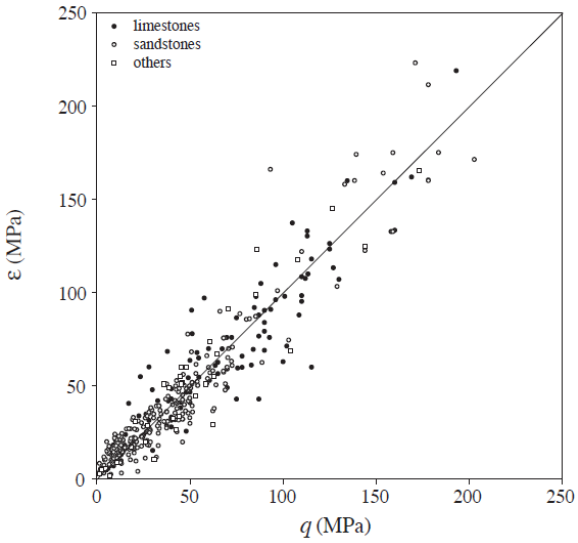

Figure 10. Cross plot of intrinsic specific energy ε (ISE) versus uniaxial compressive strength q (UCS) of variable lithologies (Richard, et al., 2012).

The orientation of the core azimuthally, when performing scratch test, results in different strength values (Epslog, 2018). A personal communication with Epslog representative revealed that strength measurements is dependent on shale bedding, as per their study experiment.

Epslog's study experiment was conducted on a wax-preserved one-foot-long core. Upon removing the wax, the core appeared dry on the outer surface. Eight scratch trials were performed with 45 degrees of azimuthal spacing between them (Figure 11). The experiment revealed that strength values depend on bedding orientation of shale, which most probably linked to shale anisotropy. Similarly, in UCS, different samples were extracted in different angles with respect to bedding. Theses samples were tested with UCS to capture the UCS's range of values as plug orientation varies with bedding. Both experiments, UCS and Scratch, showed a similar ratio (of ~2) between the maximum and minimum values.

In this study, no shale bedding dip information or scratch azimuth were collected. Also, even though the orientation of the UCS plugs are known (vertical), the angle with respect to the bedding is unknown. However, the UCS and scratch values show a close match. Also, most of the scratch measurements were conducted on sands, where no anisotropy was captured by the Epslog study experiment.

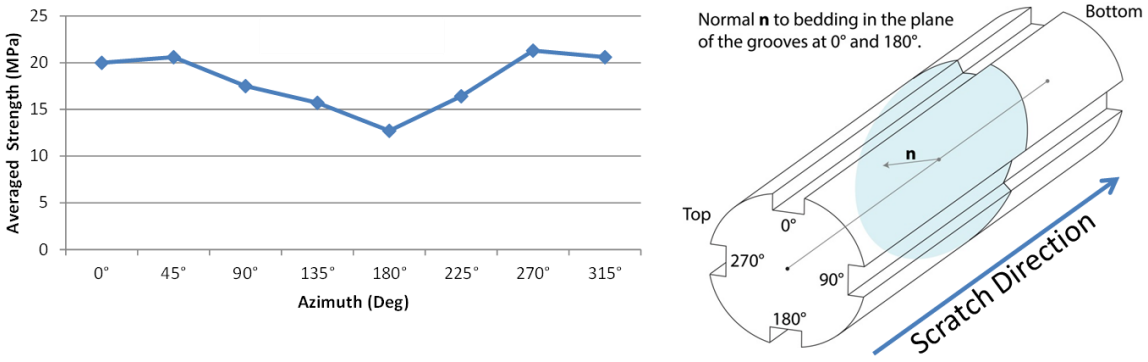

Figure 11. Azimuthal strength profile of the experiment conducted on shale (Epslog, 2018).

6.3.5. Compressive Tests

Even though the samples selected for the compressive tests sum to eighty-nine samples, the data coverage is mainly limited to the Upper Slochteren (Figure 13). Also, many samples were arithmetically averaged because of their similar or very close depths. Samples were averaged to match log resolution (~0.3-0.5 m) (Appendix 5b) (Appendix 5a). Many samples where meant for specific tests which required twin plugs (Hol, et al., 2018).

6.3.5.1. Uniaxial Compressive Strength (UCS) test

Uniaxial compressive strength is a very common test to determine rock properties and widely used in the petroleum and civil industries to compare rock strengths qualitatively (McPhee, et al., 2015). On the other hand, a UCS test is time consuming and requires sample preparation prior to the experiment. The test is conducted by applying a load on a core plug and records the stress and strain data until the plug is fractured. That maximum stress recorded is when the sample is fractured and will be considered as the UCS value for that sample. Figure 12 shows a general setup of the UCS experiment.

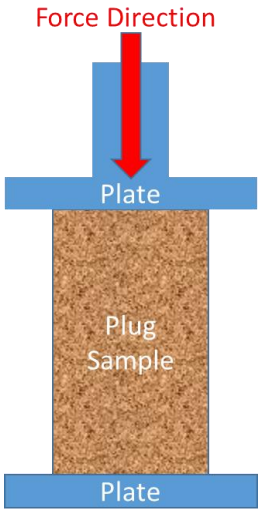

Figure 12. Schematic drawing of the UCS experiment setup.

A total of 24 samples have been tested with UCS. Fifteen samples were from ExxonMobil (Appendix 4a) and nine from NAM (Appendix 4b). The number of samples cover good section of the Ten Boer and Upper Slochteren, however, at the time of writing, the Carboniferous section is under-sampled, with only two UCS sample points. Sample selection covered a variety of lithology, clean sands, dirty sands and clays (Figure 13).

6.3.5.2. Triaxial Compressive Strength Test (TCS) and Elastic Properties

Triaxial compressive test provides more information regarding the mechanical elastic properties when compared to the conventional compressive tests, UCS, since it accounts for radial boundary conditions and parameters. The triaxial dataset was produced by the ExxonMobil lab. The total number of samples were fifty-three, of which thirty-eight were vertical. Only the vertical samples are used in this study.

The test is performed by loading a cylindrical sample with an axial stress to a pressure difference Q of 3000 psi, or 20.7 MPa (Equation 9). Then, the sample is unloaded from Q values of 3000 psi (20.7 MPa) to 1000 psi (6.9 MPa) where the elastic parameters of Young's modulus and Poisson's ratio are measured.

These parameters are measured during the unloading stage to capture the material's properties during an elastic behavior. During the experiment, constant radial and pore pressure are maintained. However, the sample is allowed to strain radially as well.

$$Q = P_{ax} - P_{rad} \tag{9}$$

P_{ax}= Axial stress (MPa or psi)

P_{rad}= Radial stress (MPa or psi)

6.3.5.3. Uniaxial Strain Compression Test with Pore Pressure Depletion and Elastic Properties

Uniaxial strain experiments, performed in labs Shell, were used to measure axial compressibility. The tests were performed with a pore pressure depletion protocol. Twenty-seven vertical samples have been tested.

The test is conducted by loading a cylindrical plug to the reservoir's initial conditions with a pore pressure of 35 MPa for 24 hours. Later, the sample undergoes three different pore pressure depletion stages, while maintain constant axial stress and variable radial stress to eliminate radial strain. Three unload and reload cycles were performed in every stage. In stage one, pore pressure was varied through three unload and reload cycles between 30 and 25 MPa. Stage 2 varied between 19 and 14 MPa. Stage 3 varied between 8 and 3 MPa. Vertical uniaxial compressibility was measured during each stage and Young's modulus and Poisson's ratio were calculated (Hol, et al., 2018). Even though the sample was not allowed to strain radially, Young's modulus and Poisson's ratio were estimated using linear poro-elastic theory.

Young's modulus, E, is defined by dividing stress over strain (Equation 10) from lab experiments. Young's modulus is related to the material's stiffness, where higher values mean stiffer material. Compressibility describes the relation between pressure applied on a body and the resulted volume change (Zimmerman, 1990) (Equation 11). The inverse of compressibility means the material's resistance to compressibility, which is described as bulk modulus K.

$$E = \frac{\sigma}{\Delta L} \tag{10}$$

$$\frac{1}{C_m} = K = -V\,\frac{\partial P}{\partial V} \tag{11}$$

σ = Applied stress (MPa)

ΔL = Strain (m)

V = Bulk volume (m^3)

P = Applied stress (MPa)

C_m = Compressibility (1/MPa)

K = Bulk Modulus (MPa)

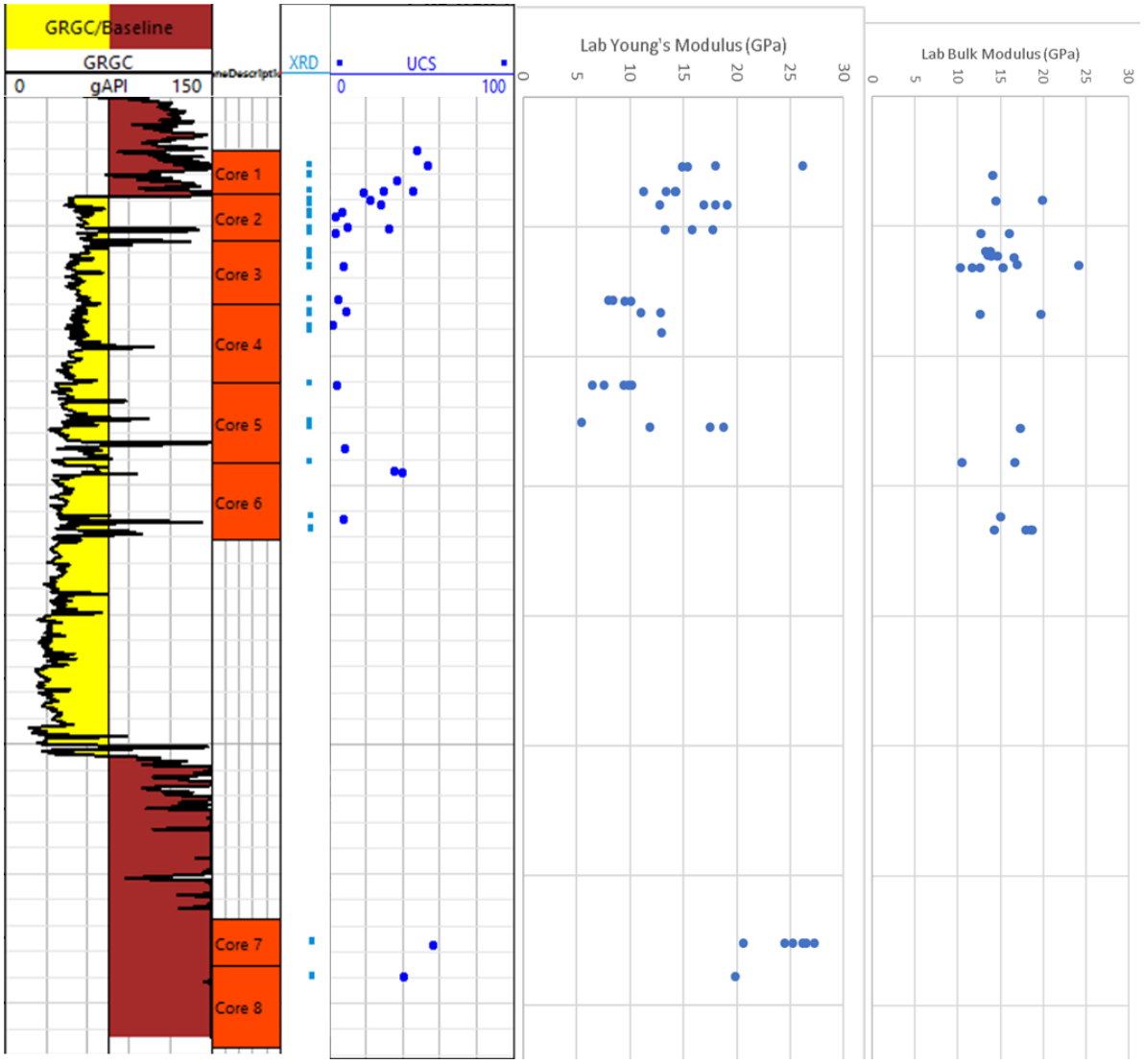

Figure 13. Distribution of the plug samples that were tested for XRD and UCS and TCS (Young's modulus and Bulk modulus) tests with values.

6.3.6. Special Core Analysis (SCAL)

6.3.6.1. X-Ray Diffraction (XRD)

X-ray diffraction (XRD) was discovered in 1912 by Von Laue after he noticed crystals diffraction of X-rays differently. This method is useful for identifying the mineral composition of rock samples since each mineral has different crystal lattice structure (Cullity, 1978).

A total of 49 samples were examined with XRD by Shell, 23 samples, and ExxonMobil, 26 samples (Appendix 6b and Appendix 6a). Sample analysis returned a detailed mineral composition that can be used for cross checking any later analysis. Figure 13 shows the distribution of samples that undergone XRD analysis.

6.3.6.2. Computed Tomography Scan (CT-Scan) and Hounsfield Number

Computed tomography (CT) was developed by Sir Godfrey Hounsfield in 1972 for medical purposes. This non-destructive method uses the linear attenuation coefficient (μ) of the material with respect to water (Equation 12), with air being -1000 and water is 0 and the number increases as density increase (Cantatore & Müller, 2011). The Hounsfield number is then converted to a gray scale, or CT, image. The CT-scanning of the core is continuous. Since the variability in the color-scale of CT scan images essentially depends on the variability of the density, it maybe be used as a proxy to density and can be compared with density logs, providing a link between the wireline log and the core info.

$$HU = 1000 * \left[\frac{\mu - \mu_{water}}{\mu_{water} - \mu_{air}}\right] \quad (12)$$

7. Data Analysis and Preparation

The previously mentioned dataset was used in the following steps to be carefully analyzed and prepared for further quantitative or qualitative analysis. The following steps can be considered as part of the methodology. Techlog® from Schlumberger and RokDoc® from IkonScience® will be used to produce interpretations or calculations.

7.1. Data Depth Matching

Electrical logging data acquisition, wireline in this case, is performed by lowering the logging tools with a cable string. The common practice is to start collecting data starting from the bottom to the top of the desired section to be logged. As the tools are being pulled out of the hole, the speed of the pulled tools is inconstant, mainly due to stick and slip, and may cause depth offset in measurements between different logging runs (Major, et al., 1998). Usually, quick and dirty log-log depth matching is performed on well site by stretching and squeezing logs to match other logs' signatures with log signatures from gamma ray. However, a detailed depth matching is necessary to ensure alignment of log signature responses for this work.

7.1.1. Log-log Depth Match

Log-log depth matching was performed on all logs to match the gamma ray logs signatures. First, density and shear acoustic logs were used to match their signatures with gamma ray since they showed higher dependency of gamma ray. Then, the depth shift table of gamma ray and density was used on neutron porosity log. The depth matched density was then used to match compressional acoustic. Resistivity log showed good match with gamma ray, therefore, no depth matching was performed on resistivity. Figure 14 shows some of the obvious mismatches found on the logs.

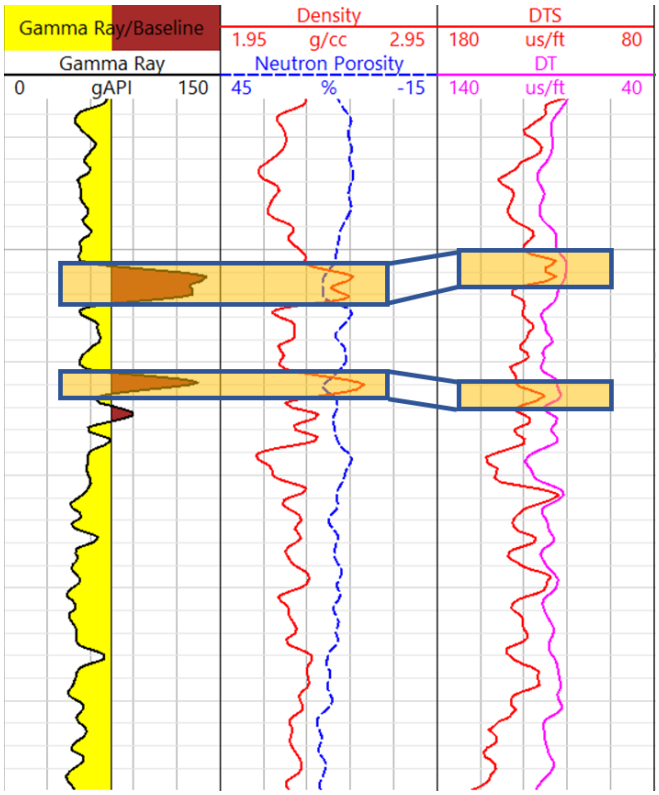

Figure 14. Raw electrical logs showing some of the encountered mismatches between logs signatures.

7.1.2.Log-core Depth Match

Core depths are usually recorded by driller's depth, which is usually not in accordance with wireline depths, and they need to be depth matched with logs because wireline depths are corrected for cable stretching while drill pipes are not. The core dataset represented in RCAL, CT-scan, petrography and scratch test were depth-matched with depth shifted density.

7.2. Curve smoothing

The dataset available for the project came from different sources and variable depth sampling rate/depth resolution. Wireline log resolution are overall close to each other, about 30-50 cm. However, data from core analysis had a wide range of resolutions. Hounsfield number from CT-scan had a resolution of about 1-2 mm. Therefore, Hounsfield number was resampled to 50 cm. (Figure 16). The scratch values/logs that were provided by Wombat™ machine had different depth resolution outputs to choose from, 1 cm, 5 cm, 10 cm, 50 cm, 100 cm and 200 cm. 50 cm resolution was found to show a similar signatures and events when compared to electrical logs (Figure 15).

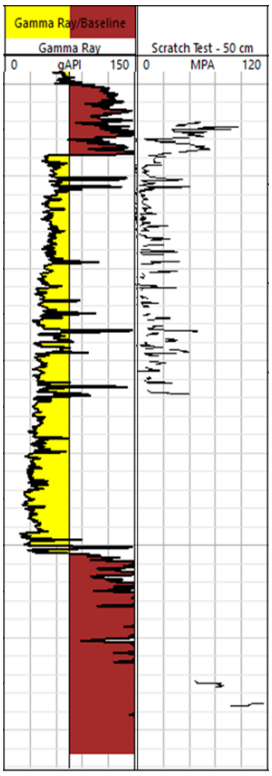

Figure 15. Output data from Wombat™ scratch test machine with 50 cm resolution curve.

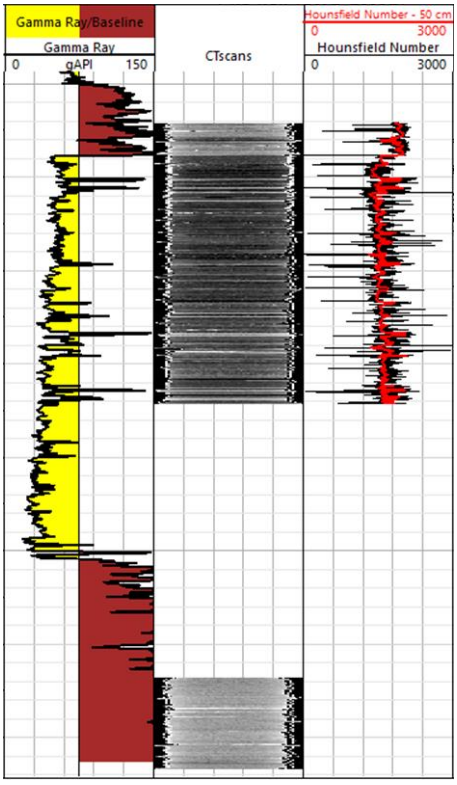

Figure 16. CT-scan image and Hounsfield number. Red curve is the smoothed Hounsfield to 50 cm resolution.

7.3. Clay Volume Calculation and Calibration

The clay volume (V_{clay}) was interpreted for the whole section using a linear interpretation (Equation 13). The equation requires user input of clean sand gamma ray and clay gamma ray values. The section was divided into four zones, Ten Boer, Upper Slochteren, Lower Slochteren and Carboniferous and each zone was assigned with different sand and clay gamma ray parameter values to calculate clay volume.

The parameters were tuned and calibrated to guide the interpretation and to produced close match between the interpreted and measured clay volume from XRD samples. Illite, kaolinite, mica and chlorite were summed to represent the clay volume in the samples.

$$V_{Clay} = \frac{GR_{Clay} - GR_{Log}}{GR_{Clay} - GR_{Sand}} \quad (13)$$

V_{clay}= clay volume (fraction)

GR_{Clay}= clay gamma ray value (API)

GR_{Sand}= clean sand gamma ray value (API)

GR_{log}= gamma ray value from log (API)

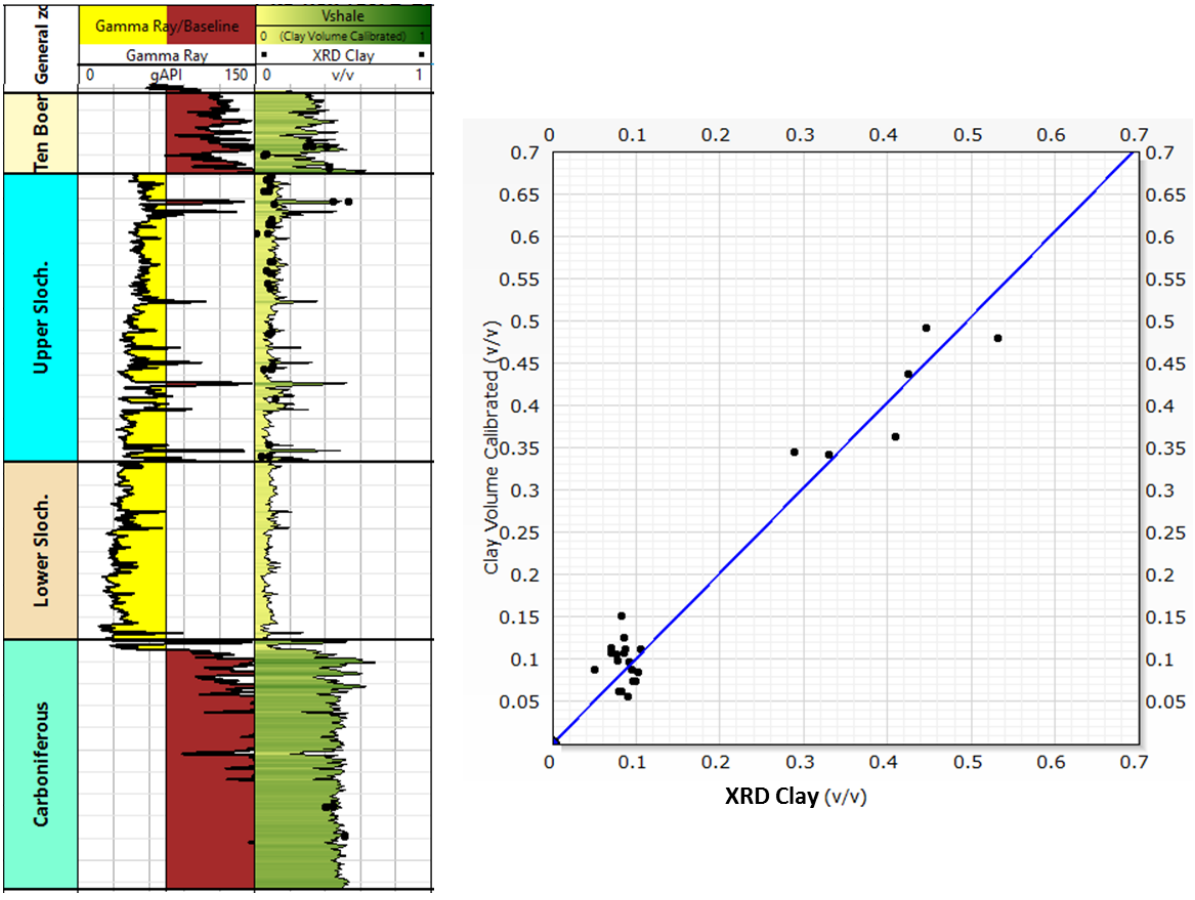

Figure 17. (left) Log view of the interpreted clay volume and the measured clay volume from XRD (right) Cross plot between the interpreted and measured clay volume.

7.4. Total Porosity Calculation and Calibration

With the availability of stressed porosity measurements, total porosity was reinterpreted, using neutron-density method, to produce a closer match with the stressed porosity. After reinterpretation, total porosity of the Slochteren and Ten Boer show very good match with the stressed porosity from lab measurements. However, interpretation of the carboniferous porosity was over-estimated by a factor of 2.0. Consequently, the carboniferous porosity was divided by 2.0 (Figure 18). The neutron-density is a generic method used to calculate total porosity. It appears that this method over-estimates the porosity in the Carboniferous.

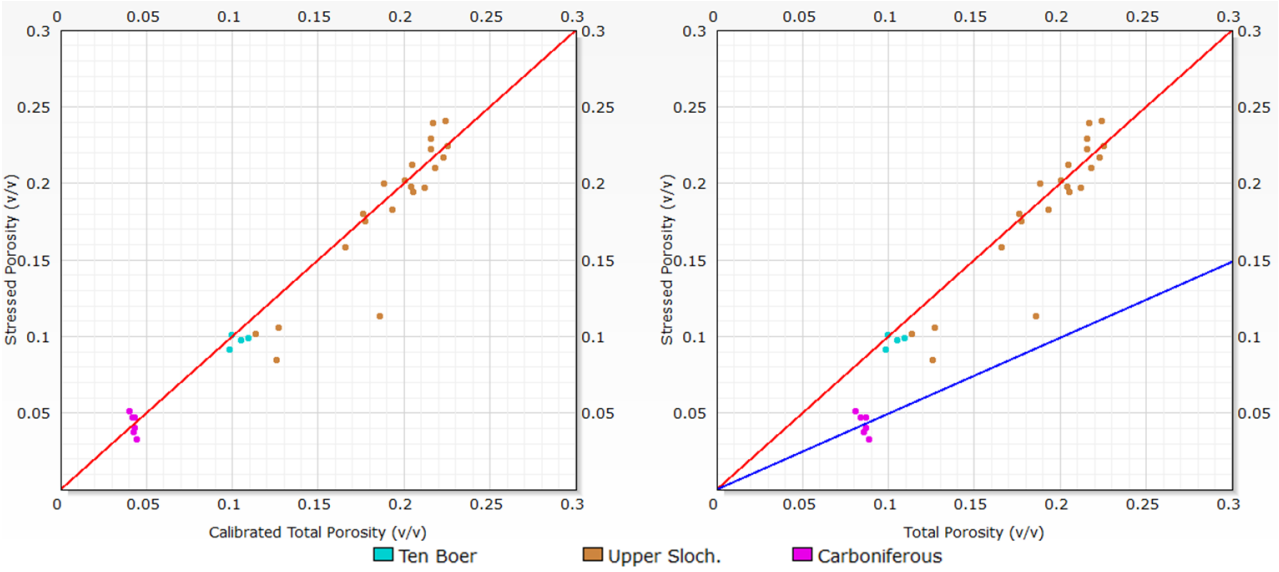

Figure 18. (left) Cross plot of lab stressed porosity and log total porosity after calibration of Carboniferous porosity with 1 to 1 trendline (right) the same cross plot before calibration. The blue trendline represents the trendline of the Carboniferous porosity data.

7.5. Formation Water Properties

Determining formation water properties is important to account for the water fluid phase. Water resistivity interpretation was performed by the NAM asset team. Using this information and Stumberger chartbook, a water salinity was found to be 300 kppm when using the water temperature and water resistivity cross plot (Figure 19). Similar value to was found from lab experiments when a sample was centrifuged.

Fluid density was interpreted to be about 1.175 g/cc when using the temperature-density cross plot as a function of pressure and salinity. Unfortunately, the cross plot doesn't show a 300 kppm with ~1435 psi (estimated reservoir pressure in 2015) trendline. Therefore, the 300 kppm and 1000 psi trendline was extrapolated linearly, using the same displacement between 200 and 250 kppm trendline (Figure 19).

Formation water salinity is on the high range. The reason could be related to the geology of the formation. Many diagenetic stages, that include carbonate and evaporites, have taken place in the formation. Therefore, dissolution of these minerals can aid in rising salinity. Another reason could be related to the structural element. An evaporitic salt layer, Zechstein formation, overlay Ten Boer. Faulting event can juxtapose the salt to the Slochteren sandstone and dissolve the salt into it.

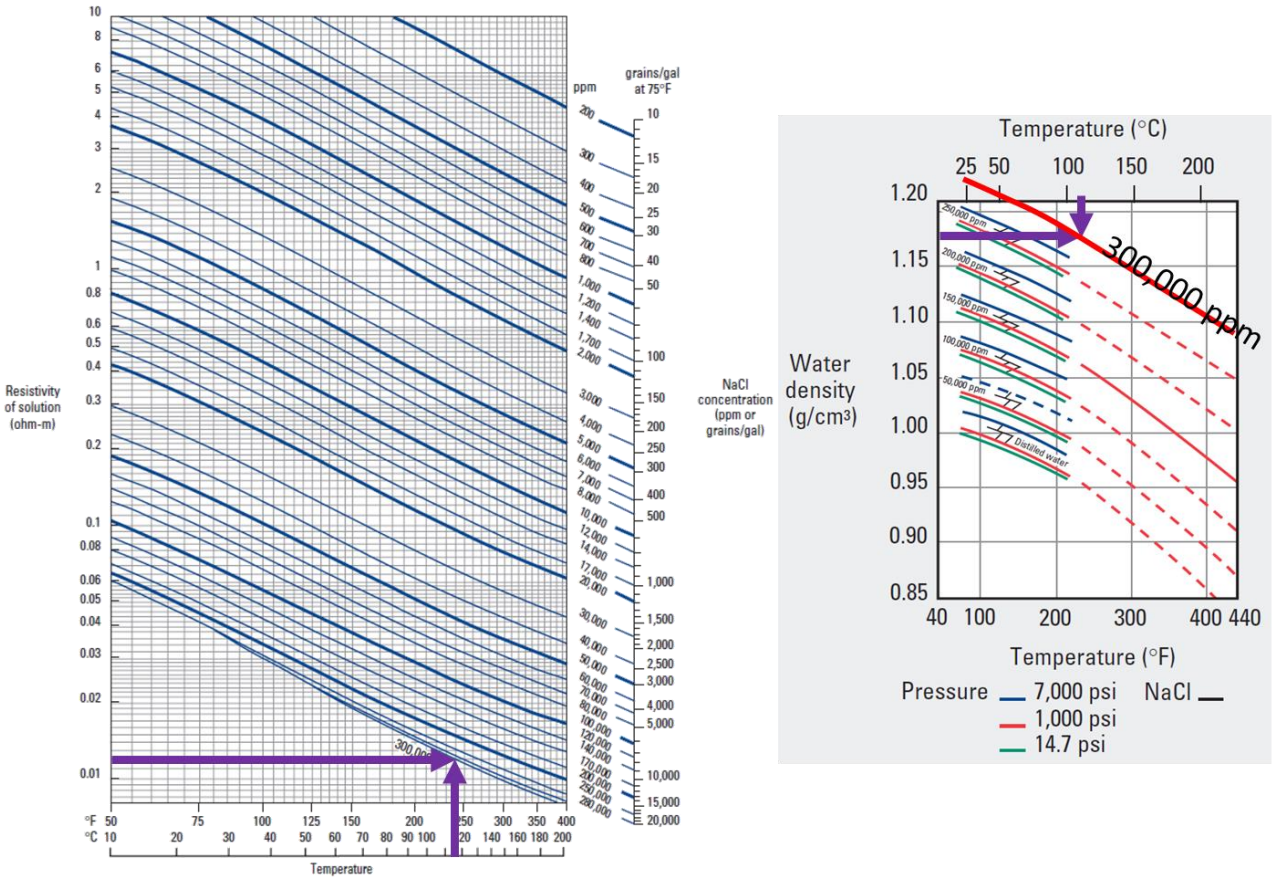

Figure 19. (left) Water resistivity and temperature cross plot indicating a 300 kppm water salinity at ~0.12 ohm.m and 114 °C (right) Temperature and density cross plot showing a 1.175 g/cc brine density.

7.6. Water Saturation Calculation

Various water saturation calculation methods can be used in reservoir formations. The common methods used are Waxman-Smith and Archie equations. Waxman-Smith is common practice for these settings since it accounts for clay conductivity. However, this method is usually used in fresh water conditions which doesn't apply in our case, 300 kppm salinity. Therefore, Archie method was used.

Archie (1942) proposed a method to use true, water filled rock and water resistivity along with porosity to calculate water saturation in clean sands. The proposed equation that employs electrical properties and porosity, in addition to three exponents, to calculate saturation (Equation 14). These exponents are: saturation exponent (n), cementation exponent (m) and "a" factor. Usually these parameters are derived from lab experiments by varying fluid compositions and measuring their resistivity (Equation 14) or recording resistivity for different rock samples (different porosities) (Equation 15). However, commonly practiced, values of m, n, and a can be input as 2, 2 and 1 if no lab measured values are available (McPhee, et al., 2015).

$$[RI]^{\frac{-1}{n}} = \left[\frac{R_t}{R_o}\right]^{\frac{-1}{n}} = S_w \qquad (14)$$

$$FF = \frac{R_o}{R_w} = \frac{a}{\emptyset^m} \rightarrow R_o = \frac{aR_w}{\emptyset^m} \quad (15)$$

By substituting equation 15 into 14, the result is Archie's water saturation equation:

$$S_w{}^n = \frac{aR_w}{\emptyset^m R_t} \quad (16)$$

R_t = Rock resistivity (ohm.m)

R_o = Rock resistivity in 100% brine saturation (ohm.m)

R_w = Brine resistivity (ohm.m)

RI = Resistivity Index (unitless)

FF = Formation factor (unitless)

Φ = Porosity (unitless)

a = Empirical constant (unitless)

m = Cementation factor (unitless)

n = Saturation factor (unitless)

S_w = Water Saturation (unitless)

7.7. Gassmann Fluid Substitution

During production, saturation variation through time is caused by the extraction of hydrocarbon fluids while being displaced by the water from aquifer. Therefore, acoustic responses, rock modulus, and bulk density are affected due to this alteration in the total bulk measurement, where fluid fill of the rock's void medium is changing. Thus, it is important to know how the formation will respond in terms of acoustic measurements when fluids compositions are changing.

To understand the lithology characteristics in response to fluid displacement, Gassmann fluid substitution methods was used. Gassmann F. (Gassmann, 1951) has proposed an equation (17) between the different bulk modulus in a rock. Gassmann equation has been used widely for fluid substitution. It also come in different forms as in equation (18). However, the Gassmann fluid substitution equation has its limitations. It lacks to account for mineral and fluid mixing.

$$\frac{K_{sat}}{K_{ma} - K_{sat}} = \frac{K_{df}}{K_{ma} - K_{df}} + \frac{K_f}{\emptyset\left[K_{ma} - K_f\right]} \quad (17)$$

$$K_{sat} = K_{df} + \frac{\left[1 - \frac{K_{df}}{K_{ma}}\right]^2}{\frac{\emptyset}{K_{fl}} + \frac{(1-\emptyset)}{K_{ma}} - \frac{K_{df}}{K^2{}_{ma}}} \quad (18)$$

Where,

$$K = \rho V_P^2 - \frac{4}{3} V_S^2 \tag{19}$$

$$\mu = \rho V_S^2 \tag{20}$$

While K_{df} is solved by the following relation (Zhu & McMechan, 1990):

$$K_{df} = \frac{K_{sat}\left[\emptyset \frac{K_{ma}}{K_{fl}} + 1 - \emptyset\right] - K_{ma}}{\emptyset \frac{K_{ma}}{K_{fl}} + \frac{K_{sat}}{K_{ma}} - 1 - \emptyset} \tag{21}$$

K_{sat} = Bulk modulus of the saturated rock (Pa)

K_{df}= Bulk modulus of the rock with no fluid content (Pa)

K_{ma} = Bulk modulus of the rock matrix (Pa)

Φ = Porosity (fraction)

K_{fl} = Bulk modulus of the fluid (Pa)

μ = Shear modulus (Pa)

P = Bulk density (g/cm^3)

V_P = Compressional velocity (m/s)

V_S = Shear velocity (m/s)

Two mineral mixing fluid equations are mainly used. They represent bounds of the rock material, stiff (upper) bound or soft (lower) bound (Figure 20). The stiff bound is represented by the arithmetic averaging of Voigt mineral mixing equation (22) (Voigt, 1889). The soft bound is represented by the harmonic averaging used by Reuss mineral mixing equation (23) (Reuss, 1929). An average of both methods using equation (24), which is called Voigt-Reuss-Hill (VRH) average, was introduced by Hill (Hill, 1952) will be used to estimate the mineral mixing for K_{ma}.

$$K_{ma,voigt} = V_{clay} K_{clay} + V_{qtz} K_{qtz} \tag{22}$$

$$\frac{1}{K_{ma,reuss}} = \frac{V_{clay}}{K_{clay}} + \frac{V_{qtz}}{K_{qtz}} \tag{23}$$

$$K_{ma,VRH} = K_{ma} = \frac{K_{ma,reuss} + K_{ma,voigt}}{2} \tag{24}$$

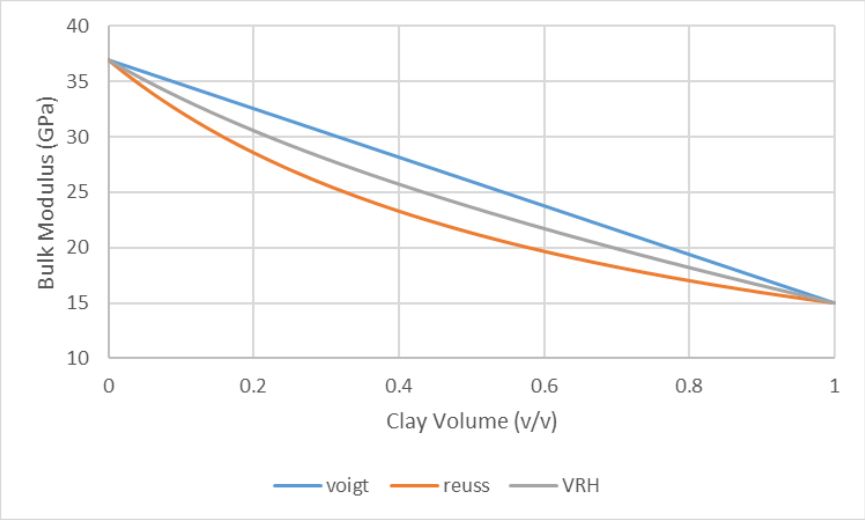

Figure 20. Bulk modulus of a clay-sand mixture using Voigt, Reuss and VRH averaging methods.

Fluid mixing will be performed using Wood's averaging equation (25) (Wood, 1955). This method averages the fluid modulus of a multi component fluid harmonically.

$$\frac{1}{K_{fl}} = \frac{S_H}{K_H} + \frac{S_w}{K_w} \tag{25}$$

S_H = Hydrocarbon saturation

K_H = hydrocarbon fluid bulk modulus

S_W = Water saturation

K_W = hydrocarbon fluid bulk modulus

Software RokDoc® from Ikon® was used to apply these equations and to produce an estimated measurement of the rock properties when the gas is substituted with brine. Bulk density, total porosity, clay volume and compressional and shear velocities were fed into the model. VRH averaging was used to average the matrix properties. Fluids were averaged using Wood's equation (23). Reservoir pressure, temperature and salinity are 9.9 MPa, 114 °C and 300 Kppm respectively. Based on these parameters, fluid properties such as density, acoustics and moduli were estimated by a built-in calculator in the software. Figure 21 shows the logs before and after correction.

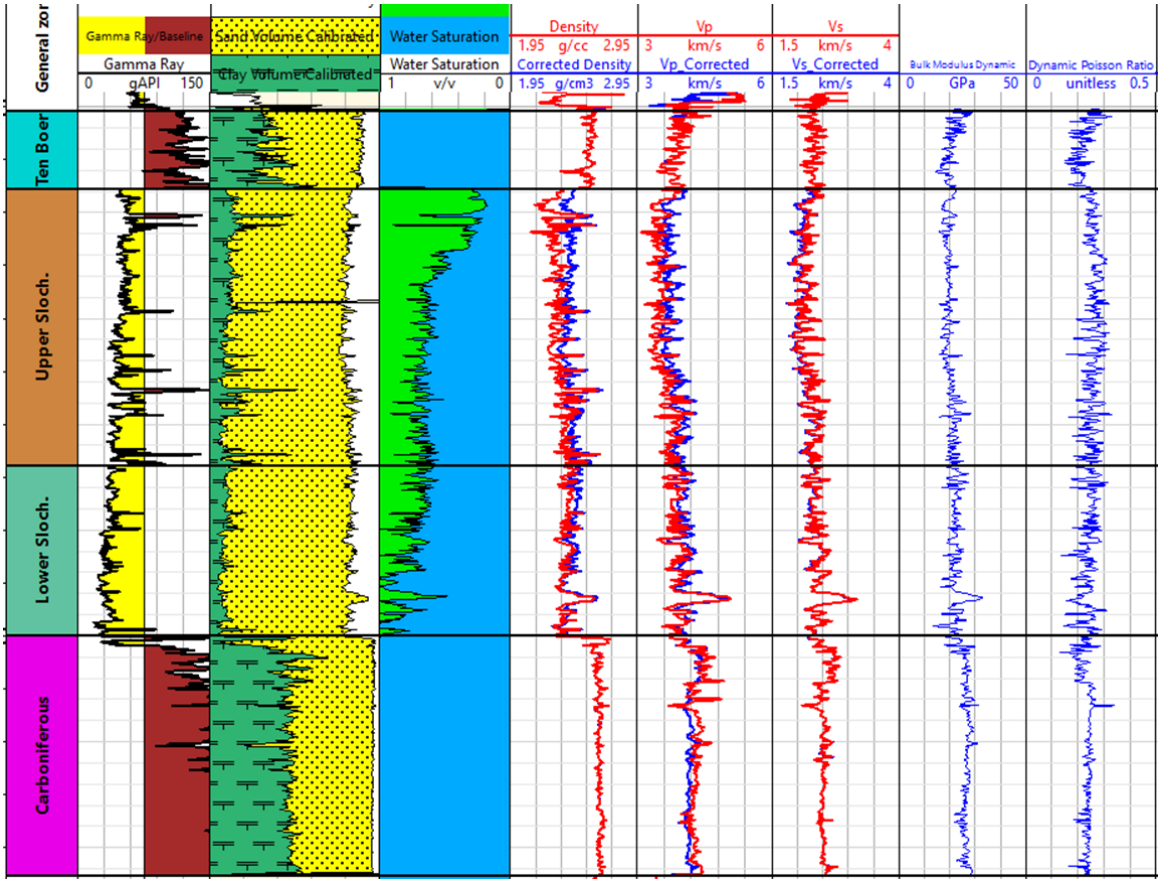

Figure 21. Log view of the density and compressional and shear velocities before (red) and after (blue) fluid substitution along with fluid and lithology composition. Also, post fluid substitution dynamic elastic bulk modulus and Poisson's ratio. The presented sand and clay volumes are calibrated with XRD and the calibrated porosity is colored in white.

7.8. Dynamic Elastic Properties Calibration

Many reports in the literature report differences between lab measured static elastic properties and log derived dynamic elastic properties (Jizba & Nur, 1990) (Nieto & Yale, 1991) (Yale, 1993). The reasons are believed to be related to data frequency contrast between the static and dynamic measurements, viscoelastic properties (micro fractures), liquid saturation effects and deformation amplitude (Yale & Jamieson, 1994). Hence, dynamic elastic properties should be calibrated.

The measured, or calculated, elastic properties from lab experiment on core are Young's modulus, bulk modulus and Poisson's ratio. Only the elastic properties measured from the unloading cycles were used for calibration since the material at that stage behaves elastically (Hol, et al., 2018). Some of the plug locations were within up to 10 cm proximity. Therefore, the elastic properties of these plugs were arithmetically averaged to reduce noise and to match log resolution, ~0.5 m. The correspondent dynamic properties, which were estimated after Gassmann fluid substitution, were plotted against the lab measured elastic properties to find a relation that can be used for calibration. Young's modulus was calculated using equation 26. After cross plotting, correction factors for the dynamic Young's modulus, Poisson's ratio and bulk modulus were 0.59, 0.97 and 1.13 respectively.

$$E = \frac{9 * K_b * \mu}{3 * K_b + \mu} \tag{26}$$

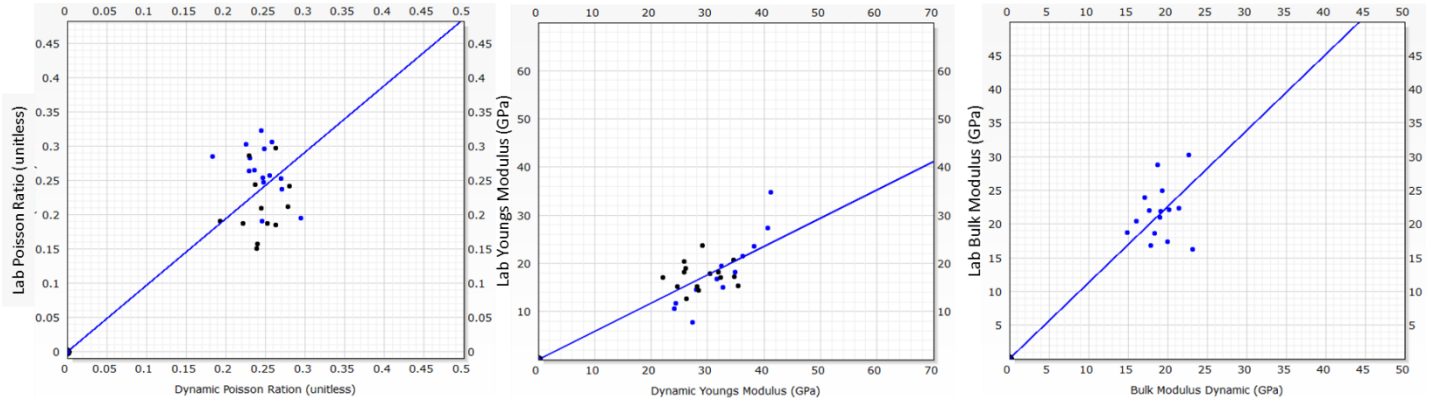

Figure 22. Dynamic elastic properties vs lab's static elastic properties. (left) Log dynamic vs. lab's static elastic Poisson's ratio resulted in a correction factor of 0.97 (middle) Log dynamic vs. lab's static elastic Young's modulus resulted in a correction factor of 0.59 (right) Log dynamic vs lab's static elastic bulk modulus resulted in a correction factor of 1.13.

From the cross plots in Figure 22, Bulk modulus and Young's modulus showed more linear correlation trend between the lab and log information. However, Poisson's ratio plot is sparser and didn't show a clear trend.

7.9. Log Reconstruction

Acoustic logs from wireline tools haven't recorded a proper and full measurements of the carboniferous shale. Approximately, the bottom one-third of the Carboniferous section is suffering from this issue. Also, scratch test measurements only cover, partially and discontinuously, the cored intervals. Therefore, Techlog®'s K.mod option tool was used to reconstruct the missing parts of these logs by using information from the other logs. K.mod is a non-deterministic method to construct logs with missing data. The method creates non-linear relations between the input variables through several learning cycles to produce a result (Techlog, 2016).

7.9.1.Shear and Compressional Acoustic Log Reconstruction

The propagation of acoustic waves through formation materials is related and can give information about compressibility, mineral composition, porosity, fractures and density. Many correlations can be found that related acoustics to these parameters (Hicks & Berry, 1956) (Wyllie, et al., 1956) (Geertsma, 1961) (Raymer & Hunt, 1980). Therefore, from the available log dataset, porosity, density and clay volume were used as input variables in K.mod to reconstruct the acoustic intervals.

In the log reconstruction process of the missing parts of acoustics, only the acoustic measurements within the Carboniferous section was selected. The reason was to use only acoustic responses of shales to interpret the missing parts of the Carboniferous shales. Figure 23 shows the raw and reconstructed acoustics of the Carboniferous.

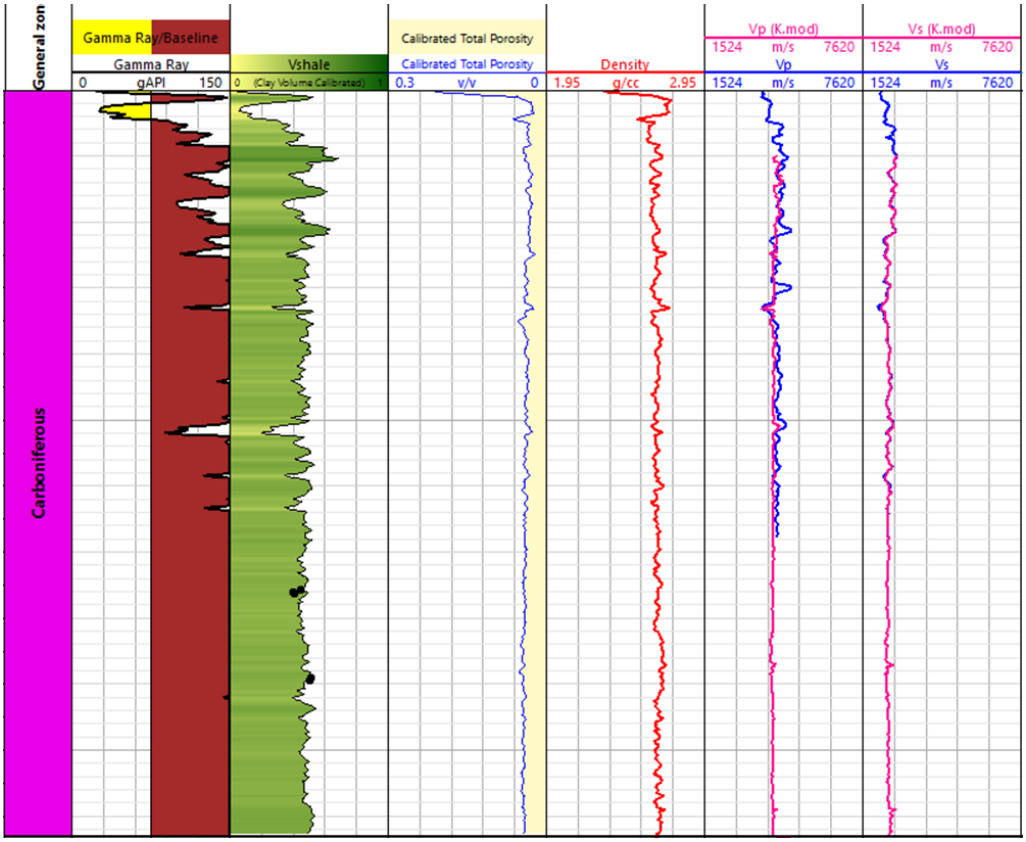

Figure 23. Log reconstruction of compressional and shear acoustics (represented in velocity m/s units) using K.mod.

7.9.2.Scratch Test Reconstruction

Scratch test only appears in the cored intervals. Moreover, scratch test can only be conducted in consolidated and not-fractured core. For this reason, scratch can be seen discontinuous in the cored intervals. The intrinsic energy recorded from scratching is proportional to UCS values with a one-to-one relation (Ferreira, et al., 2016). Mechanical properties depend on factors such as mineral composition, acoustics, density and porosity (Hol, et al., 2018) (Rashed, et al., 2014) (Sardar, 1993).

Continuous logs have been used as input to reconstruct the scratch test. Corrected compressional and shear velocities, corrected density, clay volume, porosity and neutron porosity logs have been used to reconstruct a full and continuous scratch test of the section while using the existing scratch log as a validation in the process. Figure 24 show the reconstructed scratch log.

To verify that the reconstructed scratch test was within close range of the lab scratch, Figure 25 shows a cross-plot between the interpreted scratch, from K.mod, versus the lab scratch with reasonable consistency. Also, lab UCS experiment measurements were plotted to verify the one-to-one relation.

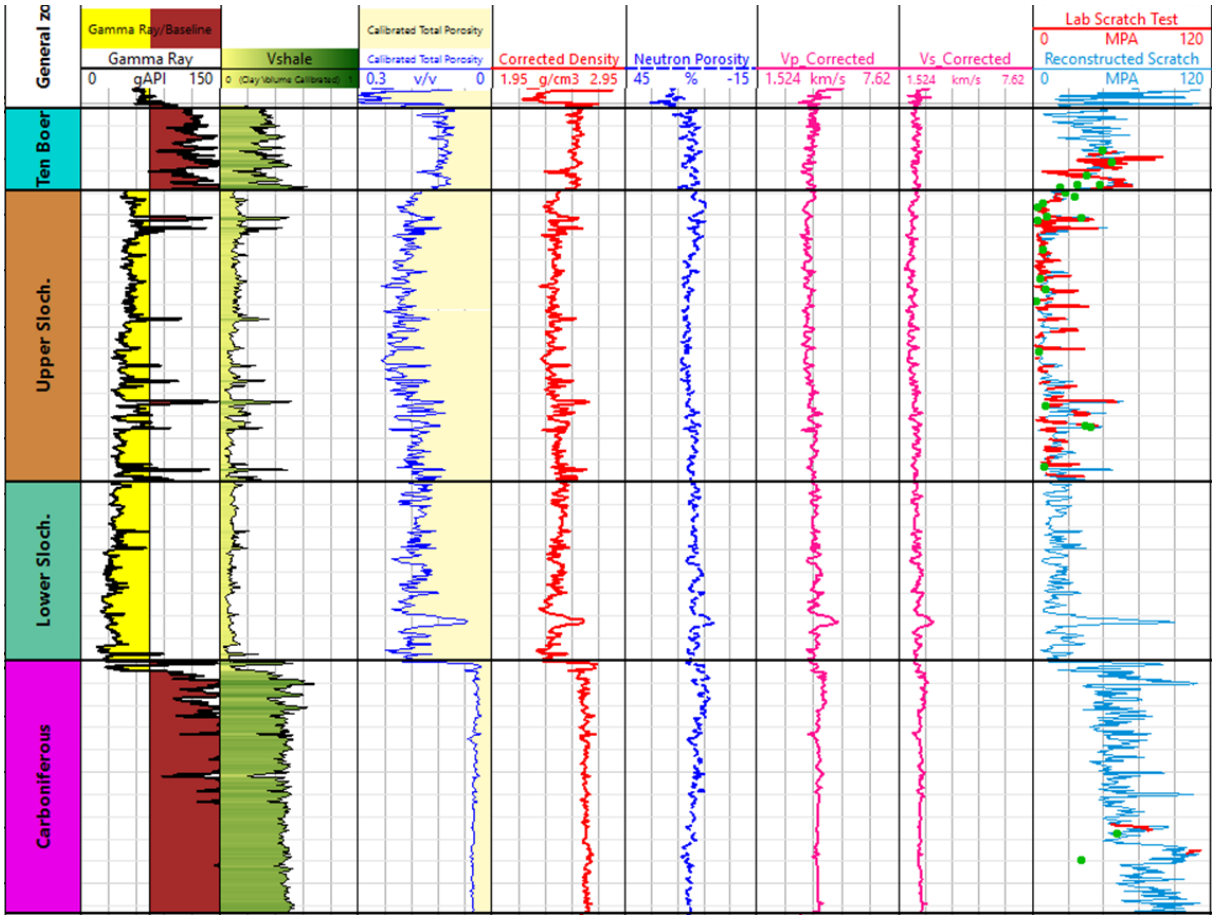

Figure 24. Input variables for K.mod (clay volume, porosity, corrected density, neutron porosity and corrected compressional and shear velocity) to reconstruct scratch log. First track to the right show the reconstructed scratch from K.mod (blue), lab scratch test (red) and UCS experiment measurements (green dots).

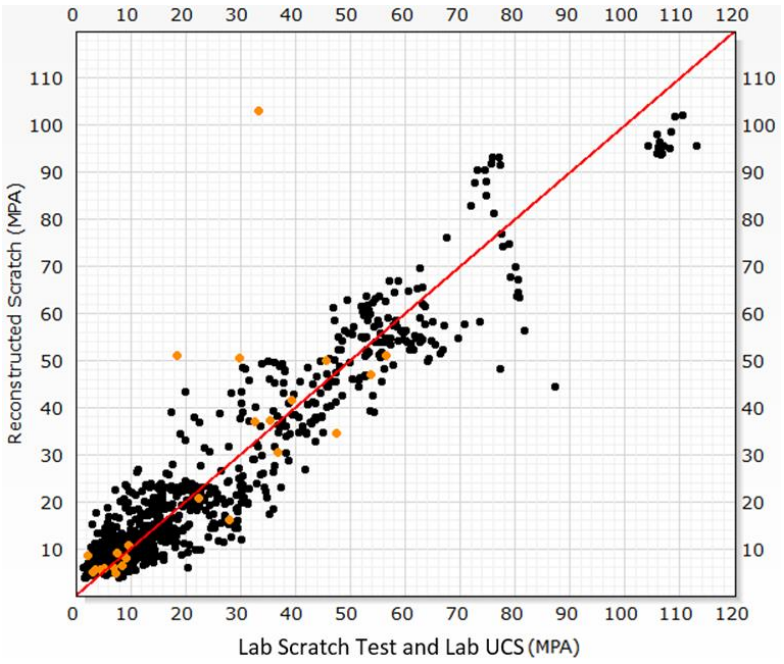

Figure 25. A cross-plot of the K.mod-produced reconstructed scratch versus the lab scratch test (black dots) and lab UCS experiment (orange dots).

8. Electro Facies Modeling and Description

With data being analyzed, prepared, corrected and calibrated, they can be used to build a model based on electrofacies using IPSOM in Techlog®. IPSOM module is based on neural network model designed for geological interpretation to predict and map/classify facies from well log data. The neural network model uses Kohonen algorithm of self-organizing (Techlog, 2016). The algorithm computes a function F, based on a real input of space A to produce space B (Rojas, 1996).

All the zones in the section, Ten Boer, Slochteren and Carboniferous shales, were selected to be modeled in IPSOM. IPSOM utilizes artificial intelligence methods for facies prediction. Fuzzy Classification method was selected after finding that it was delivering satisfactory results. The method starts after defining the input variables that will be used to perform the classification and the number of groups, or facies. Then, it goes into a loop where it calculates the groups' barycenter and finds a probability value between each node with every group (Techlog, 2016).

Several trials were conducted to find a representative number of the total facies. Six facies were found to be representative to distinguish higher reservoir quality sands, medium reservoir quality sands, low reservoir quality sands, cemented sands and two shale units.

The input variables for electro-lithological and electro-mechanical facies modeling have been selected to consider the variables used to calculate the dynamic elastic properties. Young's modulus, bulk modulus, shear modulus and Poisson's ratio equations depend heavily on density and compressional and shear velocity. Therefore, these parameters were taken into consideration in order to not use similar inputs to generate models (information redundancy).

Approximately one-third of the logged section is in the Carboniferous shales. After running many fuzzy classification models for both lithology and mechanical models, Carboniferous unit's nodes were found to

be highly clustered and show as one facies. As a result, this high data clustering will create a large barycenter in IPSOM which affects the probability distribution of the nodes. Consequently, models were run without the Carboniferous unit. Carboniferous shales were then considered to be representing one facies.

8.1. Electro-Lithological Facies Modeling

The core calibrated total porosity and the XRD calibrated clay volume logs were used to generate a lithology model. Facies classification modeling were run on Ten Boer and Slochteren. A total of five facies were found to be suitable to classify the section (Figure 26). Facies 1, 2, 3, 4, 5 and 6 represent higher reservoir quality sand, lower quality reservoir sand, dirty sand, cemented sand, evaporitic playa lake shales and deltaic shales respectively (Figure 27).

Manual assignment was necessary for facies 6 and 4. Facies 6 was manually set for the Carboniferous shales because of its highly clustered data points. In contrary, cemented sand of facies 4 was not abundant. Therefore, IPOSM was grouping it with facies 3. Thus, manual modification was performed to segregate the cements sand points from facies 3 and mark them with facies 4. Table 1. summarizes the facies classification.

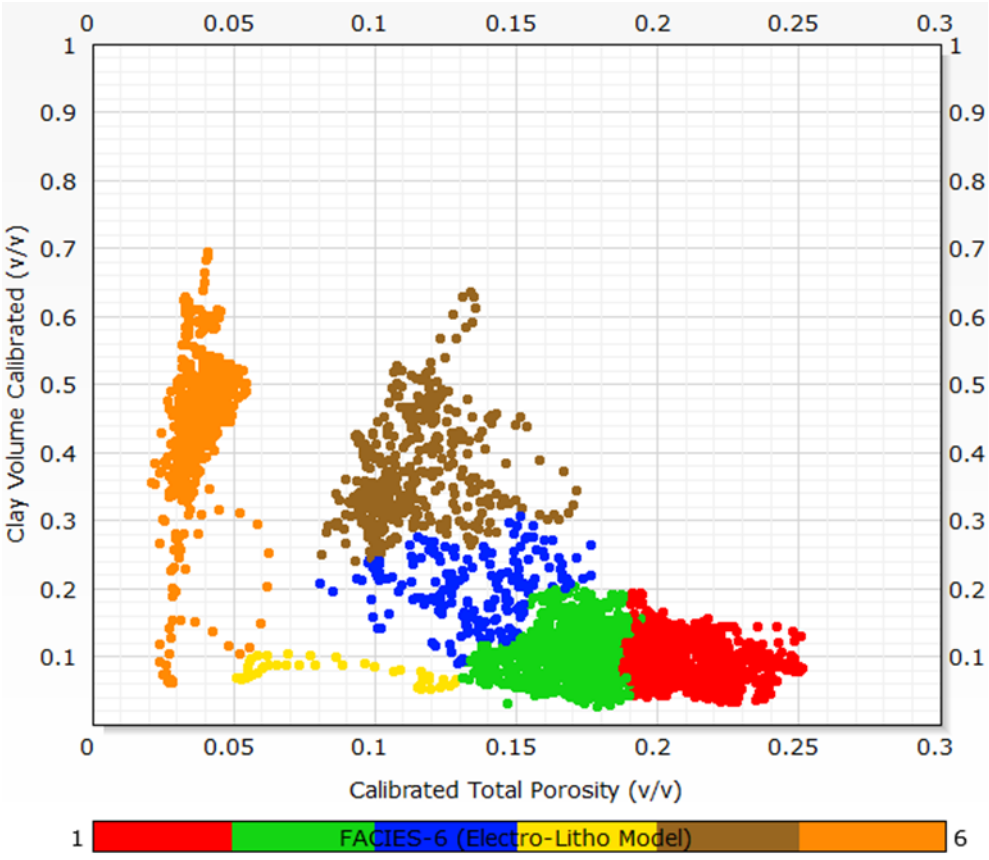

Figure 26. Clay volume vs total porosity data in a cross plot with facies color coding.

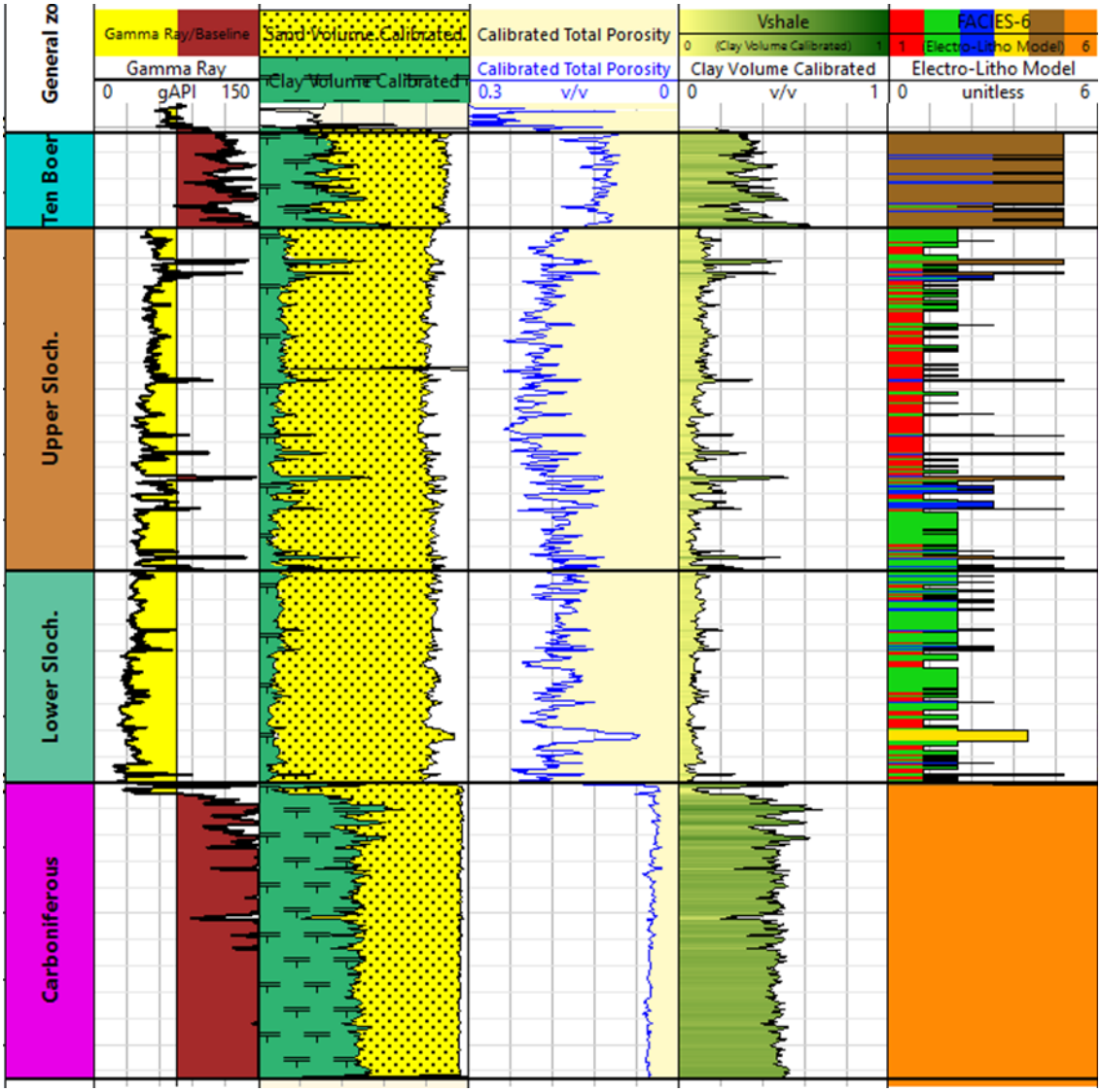

Figure 27. Log view of the electro-facies model.

8.1.1. Facies discussion and description

Sedimentological description of the core was not made available at the time of writing. However, depositional model of the Carboniferous, Slochteren and Ten Boer and facies description can be retrieved from literature. The Slochteren formation facies are mainly dominated by wadi deposits in the lower part (facies 2) and dunes in the upper part (facies 1). Other facies like evaporitic playa lake and sand/mud flats exist within proximity. Ten Boer was mainly described as restricted environment with evaporitic playa lake facies with anhydrite nodules. Carboniferous shale was described to be mainly deltaic shales (Gaupp, et al., 2000) (Gaupp & Okkerman, 2012) (Stauble & Milius, 1970).

Facies 4 is not commonly present in the section. It is interpreted as a clean and cemented sand that has very low porosity. The only appearance of this facies is in the bottom part of Lower Slochteren. Facies 3 is second to facies 4 in terms of abundance. It is interpreted as dirty sand with low reservoir quality to describe the shalier sediments and interpreted to be equivalent to sandy mudflat. Based on this information, the depositional environment of facies 1 through 6 was interpreted in table 1.

Grain analysis from LPSA on the available samples show that most of the sample selection belong to facies 1 and 2. Both facies showed a poorly sorted nature with similar geometric average of grain size (180 µm). Moreover, grain size of the facies, occasionally, can reach to a very coarse to fine gravel levels (850-1000 µm) (Figure 28). Quartz and carbonate content from XRD reveal a relation between these minerals (Figure 29). As quartz content decreases, carbonate content is a candidate for being the common cement compared to other minerals. Figure 29 show that a trendline through facies 1, 2 and 3 have a linear relation with one to one ratio between decreasing quartz content and the increasing carbonate content.

Facies number	Facies name	average porosity	Average clay Volume	Facie Description	grain size (um)	sorting
1	High reservoir quality sand	0.22	0.09	Dune	180 (occasionally 1000)	Poorly sorted
2	Medium quality reservoir sand	0.17	0.1	Wadi facies	180 (occasionally 850)	Poorly sorted
3	Low reservoir quality /Shaley sand	0.12	0.22	Sandy mud flat		
4	Cemented sand	0.09	0.09			
5	Shales	0.11	0.4	Evaporitic playa lake		
6	Carboniferous Shale	0.04	0.5	Deltaic shale		

Table 1. Overview of the lithological facies description.

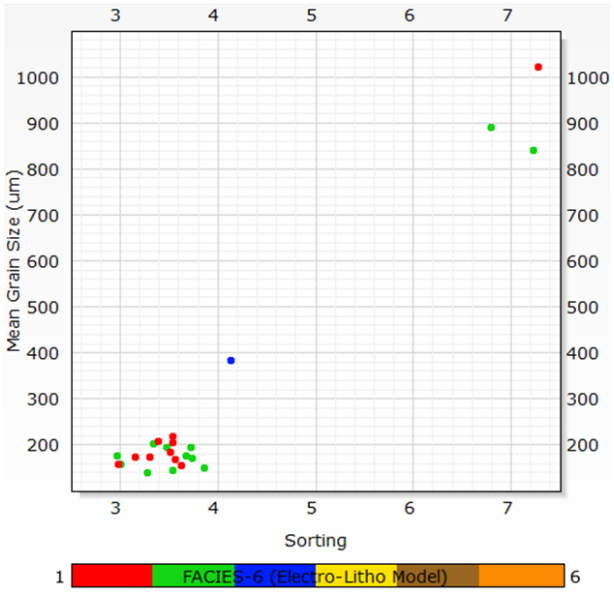

Figure 28. Mean grain size (um) vs sorting from the samples tested with LPSA colored with facies color code.

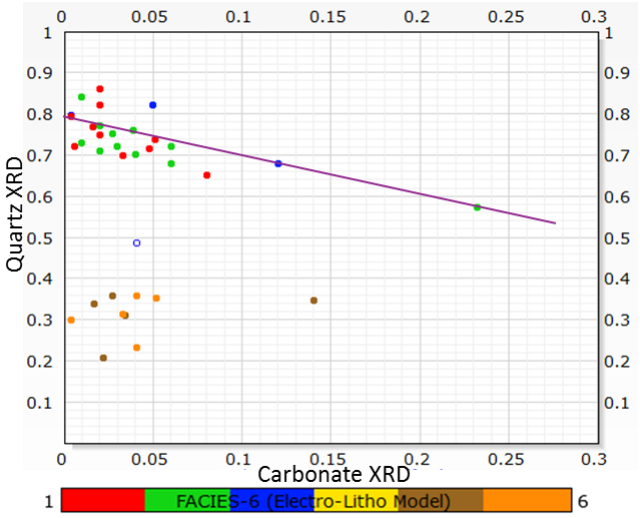

Figure 29. Quartz vs carbonate content, from XRD analysis with a trendline (purple color) across the sand facies.

8.2. Electro-Mechanical Facies Modeling

The available mechanical related logs in this study were Young's modulus, bulk modulus, reconstructed scratch log, shear modulus and Poisson's ratio (Figure 30). Different combinations of these parameters were tried to model the facies. Young's modulus, bulk modulus and the reconstructed scratch log were found to be more informative to IPSOM to perform the classification. A 6-facies model was chosen to be most representative. Higher number of facies complicates the model and creates more sub-classifications of the sands only rather than collectively sub classifying both sands and shales. Lower number of facies decreases the resolution of the model.

8.2.1. Facies Discussion and Description

Ten Boer and Slochteren zones were used in the model due to the clear distinction between them and Carboniferous shales. Facies 1 through 4, mainly representing the sand section of Slochteren, show an increasing Young's modulus, bulk modulus and scratch values. Facies 1 was found to be mainly present in the Upper Slochteren while facies 2 is mainly populated in the Lower Slochteren. Facies 3 marks the split of trendline path where Young's modulus and bulk modulus either increase for facies 4 (cemented sand) or maintain constant for facies 6 (Carboniferous). Facies 5 of the Ten Boer showed a lower Young's and bulk modulus and similar scratch values compared with facies 2 and 3 (Figure 31). A summary of the facies description can be found in Table 2.

Facies Number	Average Calibrated Bulk Modulus (GPa)	Average Calibrated Young's Modulus (GPa)	Average Scratch value (MPa)
1	17	13	8
2	20	17	16
3	23	19	30
4	30	30	70
5	19	17	45
6	25	22	70

Table 2. Electro-mechanical facies summary after calibration the dynamic properties with lab's static.

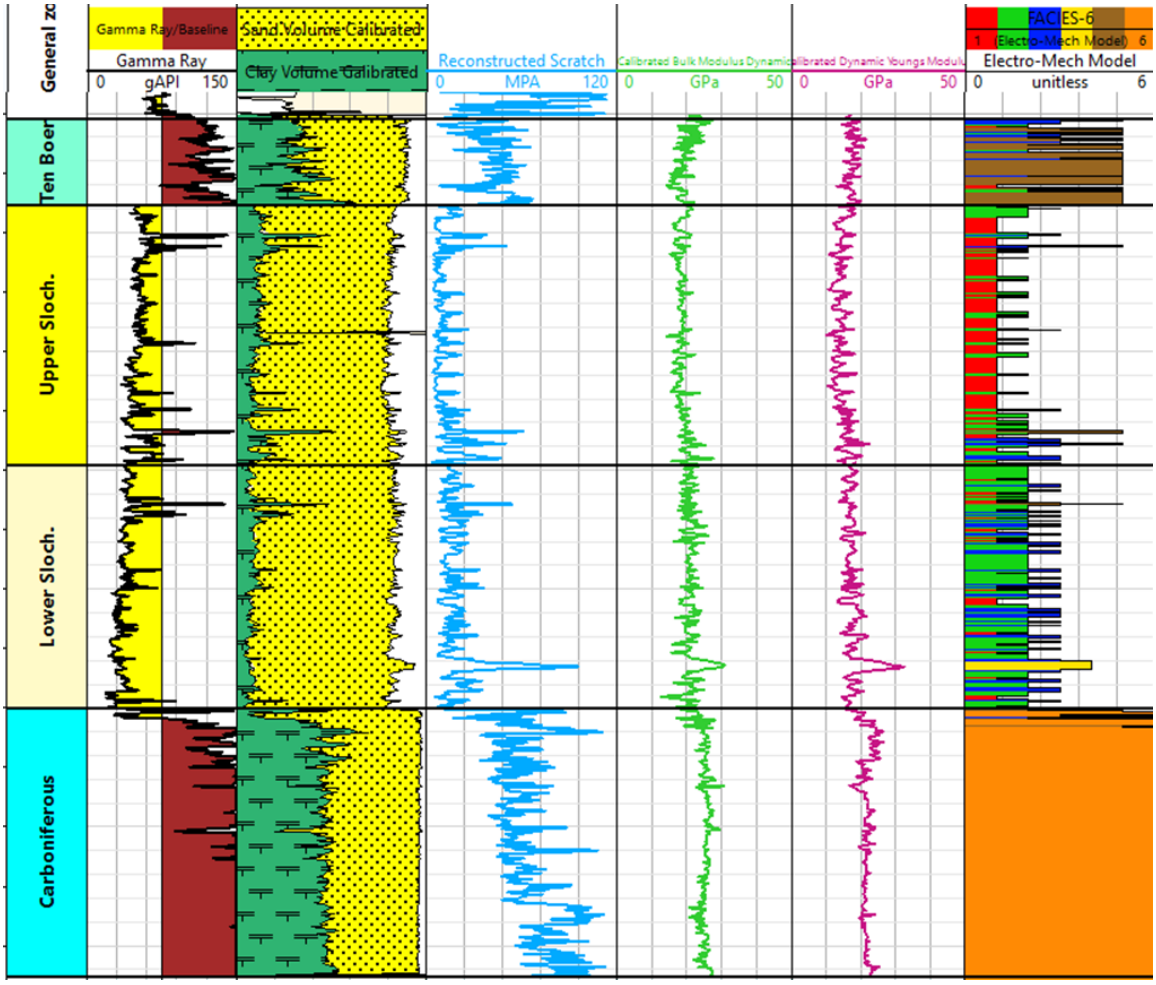

Figure 30. Log view of the electro mechanical facies model.

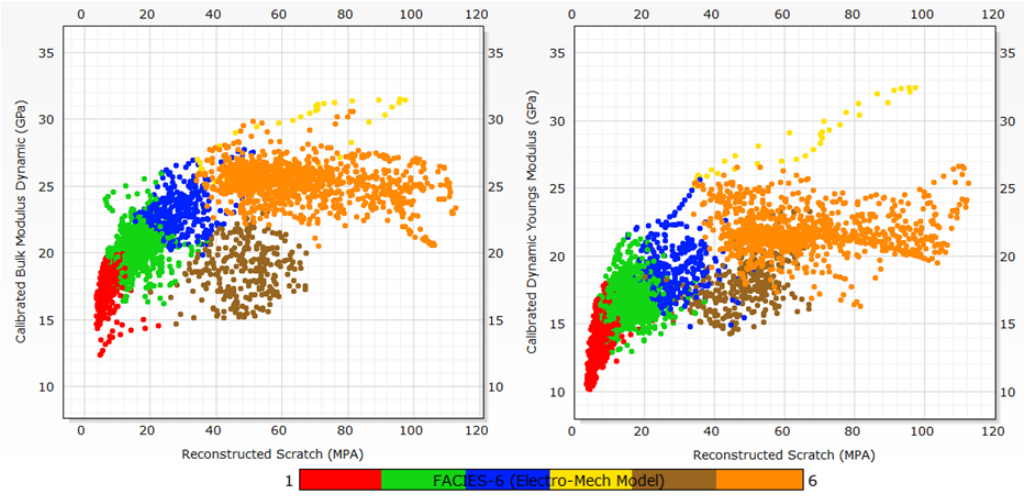

Figure 31. Calibrated dynamic elastic bulk and Young's modulus (calibrated with Lab's static elastic measurements) vs reconstructed scratch test log colored with mechanical facies code numbers.

The relationship between porosity and the compressibility factor, or it's reciprocal bulk modulus, are usually reported with each other in the literature to describe compressibility as a function of porosity (Hettema, 1996) (de Waal, 2015) (Schutjens, et al., 2004) (Schutjens, 1996). The cross-plot in Figure 32 shows two trends; one trend for facies 1, 2, 3 and 4, which are the sand facies, and one trend for facies 5 and 6, which are the shale facies.

The sand facies plot on one line independently of what facies it belongs to. Shale facies as well. An exponential trendline was chosen to fit the data. The reason the data show exponential trend is due to the squared velocities in the dynamic bulk modulus equation (Equation 19). Porosity and compressibility ranges in the study well vary from 0.05 to 0.25 and $2.8*10^{-5}$ to $6.8*10^{-5}$ 1/MPa. The breadth of the data points in sand and shale trendline show a variability range of compressibility about $1.0*10^{-5}$ to $1.2*10^{-5}$ 1/MPa (or bulk modulus of 6 to 7 GPa) at a specific porosity value.

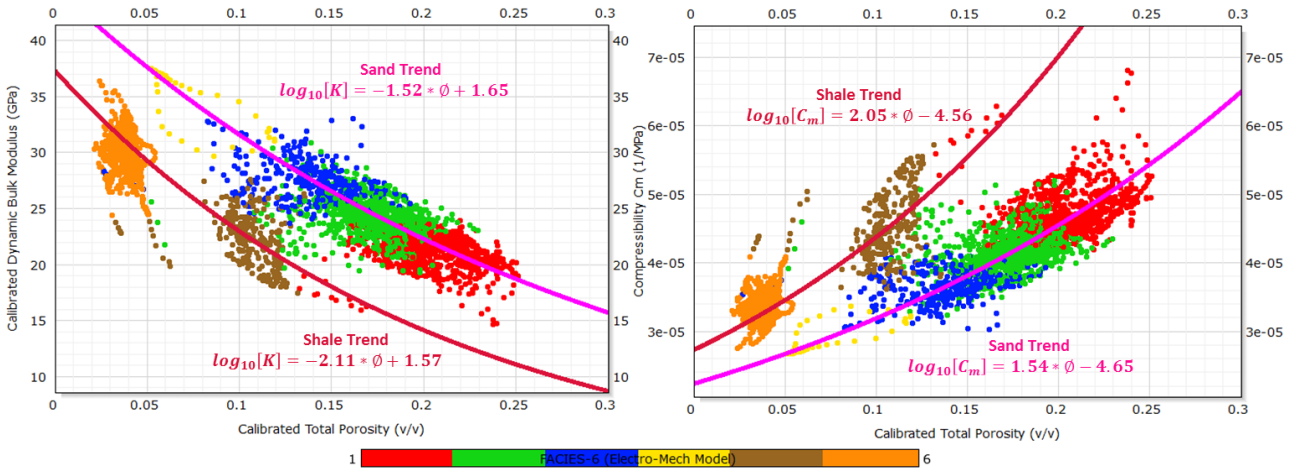

Figure 32. A cross plot of porosity with (left) bulk modulus K and (right) compressibility factor Cm colored by the mechanical facies. The pink logarithmic trendline, in both cross plots, passes through the sand facies 1, 2, 3 and 4. The dark red logarithmic trendline passes through the shale facies 5 and 6.

In Figure 33d, it can be noticed that clay content has some effect on the calibrated elastic parameters. Clay content in general increases bulk modulus, Young's modulus, and scratch test values. Using clay volumes from the XRD data, the effect of each clay component can be analyzed. Increasing content of illite, chlorite, mica and kaolinite coincides with elevated values of the calculated elastic parameters. In Figure 33, it can be noticed that elastic parameters show an increase with increasing amounts of illite, chlorite and mica content. Kaolinite doesn't show a clear trend as similar contents exist with high and low values of the mechanical parameters.

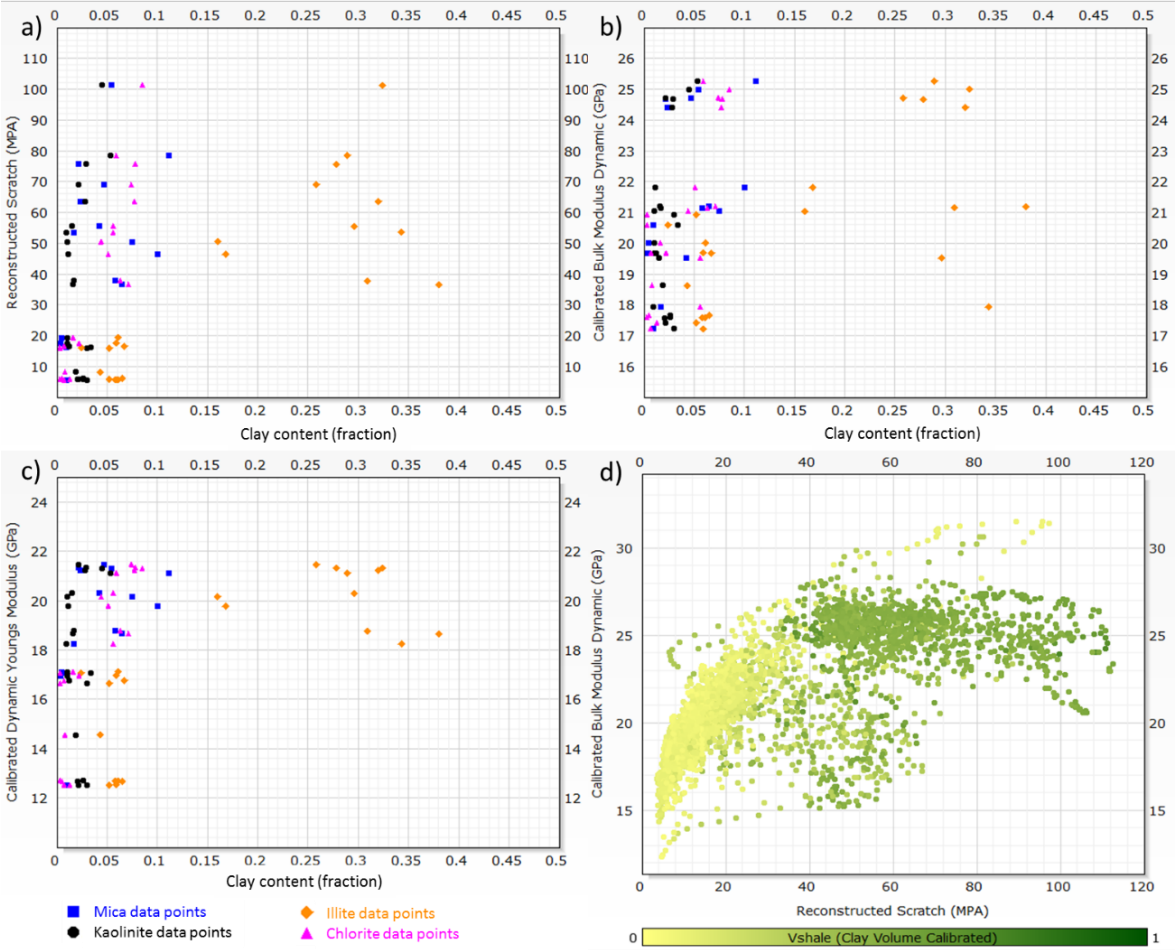

Figure 33. (a)(b)(c) Calibrated dynamic Young's and bulk modulus and scratch test vs XRD values of illite, kaolinite, mica and chlorite. (d) Bulk modulus vs reconstructed scratch colored with calibrated clay volume log.

9. Discussion

The input parameters that were used to produce both models have distinguishing information about the major units distribution in the study section. Facies 1 in both models appear to be commonly existing in the upper part of Slochteren formation while facies 2 commonly exist in the lower part. Shalier and cemented sand facies units exist minorly in streaks within the section. However, shale facies of 5 and 6 distinctively mark, lithologically and mechanically, the shales in the cap and underburden respectively (Figure 34a) (Table 3).

			Mechanical Model			Lithology Model		Comments		
Facies Number	Lithology	Facies name	Calibrated Average Bulk Modulus (GPa)	Calibrated Average Young's Modulus (GPa)	Average Scratch value (MPa)	Average Porosity	Average Clay Volume	Facies Description	grain size (um)	sorting
1	Sandstone	High reservoir quality sand	17	13	8	0.22	0.09	Dune	180 (occasionally 1000)	Poorly sorted
2		Medium quality reservoir sand	20	17	16	0.17	0.1	Wadi facies	180 (occasionally 850)	Poorly sorted
3		Low reservoir quality /Shaley sand	23	19	30	0.12	0.22	Sandy mud flat		
4		Cemented sand	30	30	70	0.09	0.09			
5	Shale	Shales	19	17	45	0.11	0.4	Evaporitic playa lake		
6		Carboniferous Shale	25	22	70	0.04	0.5	Deltaic shale		

Low	Very Good
Medium	Good
High	Fair
	Low

Table 3. Table summary of the models with descriptions

Quantitatively, an overall facies correlation achieved approximately 70% between facies 1 to 5 in both models. It means that the facies in the lithology model will match, by 70%, the facies in the mechanical model. That might lead to conclude that a lithology facies model can largely, but not entirely, replace a model using geomechanical information. More closely, when comparing each facies node in the lithology model to its opposite node in the mechanical model, facies to facies correlation ranges from 51.5% to 83% of correlation (Figure 34b). As clay content increases the correlation between the models decreases. Thus, IPSOM finds difficulty to classify a comparable lithological and geomechanical facies with higher confidence, as seen in facies 3.

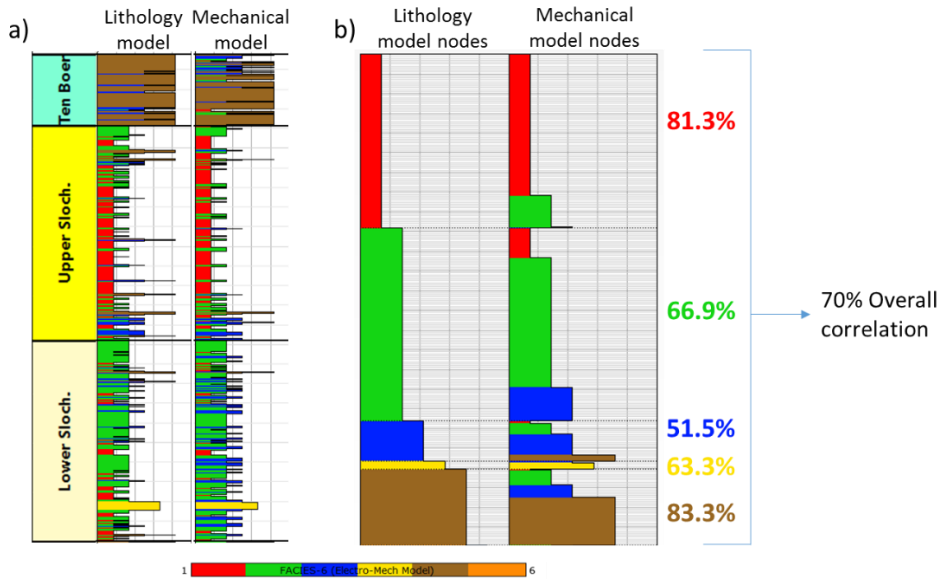

Figure 34. (a) Log view of the facies distribution across Slochteren and Ten Boer. Dominance of facies 1 in the upper slochtere, facies 2 in the lower slochteren and 5 in Ten Boer (b) Stacking of the facies nodes, in a log view, from the lithology model and its corresponding node in the mechancial model. Correlation percentage between each facies is showen with overal correlation percentage.

The current understanding of the Permian depositional model in the field area aligns with the outcome of the both distinctive (lithology, mechanical) facies models (Figure 35). A cross correlation can be established between the two electro-facies models and the human described and characterized depositional facies model. The sedimentary interpretation of Slochteren formation suggests two main facies, dune deposits in the upper section and wadi deposits in the bottom section (Glennie, 1972). This distinction is also reflected in the electro facies model. Ten Boer depositional setting is interpreted to be highly saline playa lake while Carboniferous is also a shale but deltaic. These different shale units are also distinctively captured in the electro facies model as facies 5 and 6. A sandy mudflat was reported to be present in the depositional model (Gaupp, et al., 2000). The characteristics and description of this silty lithology with mud content fits the interpreted parameters of the lower porosity and higher clay content of facies 4. Cemented facies, due to heterogeneity, were captured by Gaupp & Okkerman (2012). They interpreted the facies to be present in a very thin layers. This discerption might be comparable with facies 3. In this well, facies 3 only appears in the bottom of the lower Slochteren but in measurable thickness.

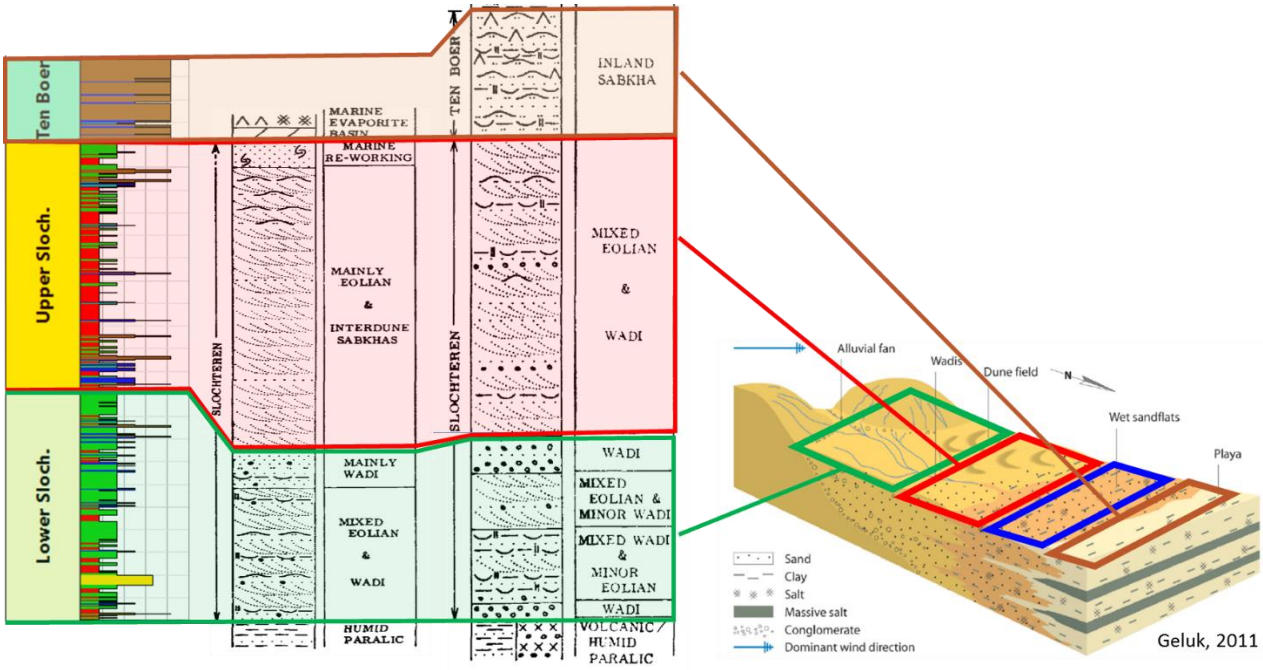

Figure 35. Correlation between the lithology model and two sedimentological descriptions from two wells in the basin from (Glennie, 1972) along with the 3D representation of the facies distribution in the sedimentology model from (Ojik, et al., 2011) and modified by (Uijen, 2013).

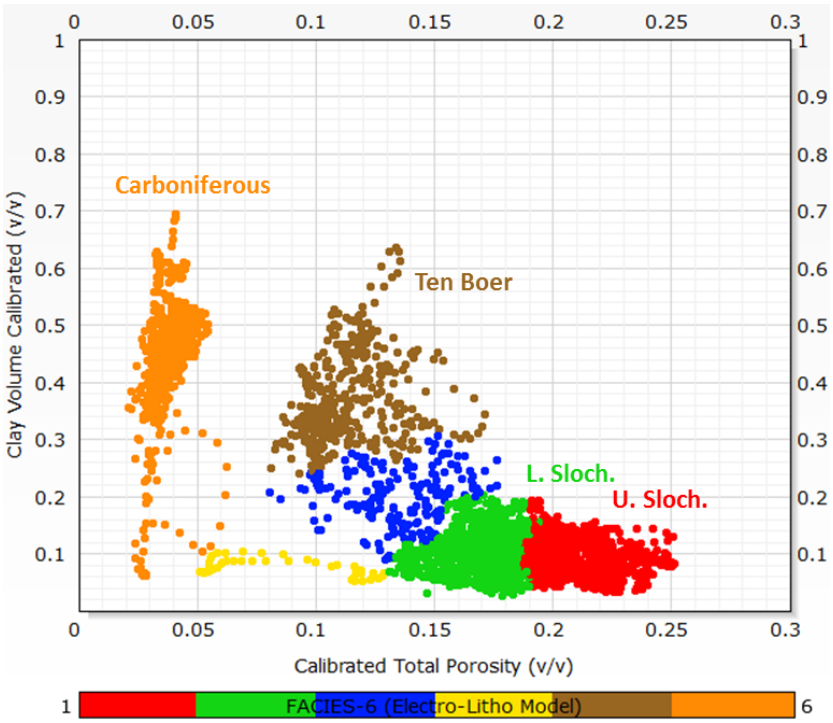

Figure 36. Data distribution in clay volume (calibrated) vs total porosity (calibrated) colored with lithology facies model. Upper Slochteren (U. Sloch.), Lower Slochteren (L. Sloch.), Ten Boer and Carboniferous are highlighted.

The wide and diverse database of spot as well as continuous mechanical measurements and electrical measurements were instrumental for this workflow. The continuous lab measured data allowed for an exemplary core-to-log calibration. The non-destructive, quasi UCS and continuous scratch test was a valuable input for the model to classify lithology qualitatively after it was calibrated with the spot UCS measurements. In addition, the use of Hounsfield number was advantageous to evaluate the corrected density and acoustics after Gassmann fluid substitution which also affects the calculation of the dynamic elastic properties.

Calibration to the interpreted logs was essential. Clay volume is a very important parameter that is calculated by using a simple linear equation with qualitative parameters determined by the user. XRD revealed its importance to be used with clay volume calibration. Based on our understanding of shales and their log signatures, the initial estimation of clay volume, without calibration, is about double what was detected by XRD. Even though Ten Boer and Carboniferous shales show a minimum of gamma ray of 100 API and up to 190 API, the XRD measured clay volume content in these formations did not exceed ~51% (Figure 37). CT scans of the plugs were examined to confirm sand content in these shale formations and validate the XRD measurements. The scans indicated the presence of sand.

Log porosity to lab's stressed porosity calibration has also been a valuable step for this study. Porosity calculation for Ten Boer and Slochteren was manageable. However, Carboniferous porosity was overestimated using wireline log interpretation alone. Lab porosity revealed that the estimated porosity by the logs were double when using neutron-density calculation method.

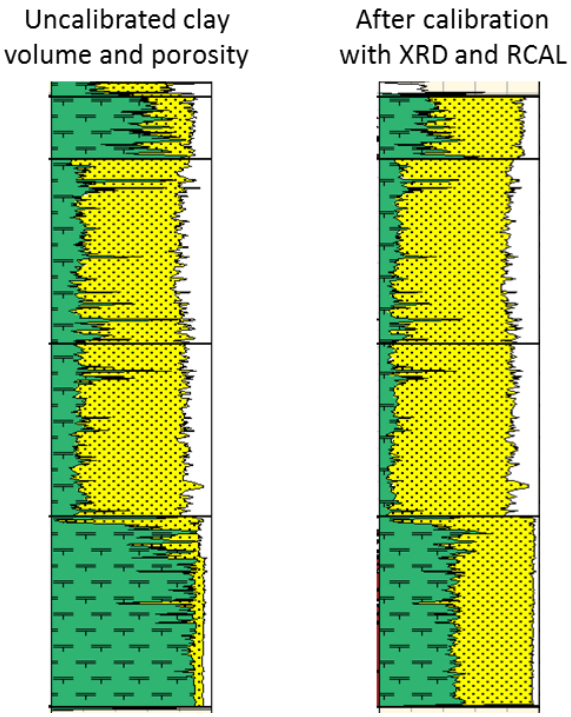

Figure 37. (left) Clay volume interpretation (green fill) and porosity estimation (white fill) before calibration with XRD and lab stressed porosity measurements. (right) Clay volume and porosity interpretation after calibration.(yellow fill is quartz)

Collectively, porosity and clay volume estimations effects can go beyond determining lithology fractions. Its effect can be seen when performing Gassmann fluid substitution to correct log acoustics and density readings. Furthermore, the output dynamic mechanical parameters are also affected because of the unrepresentative averaged lithology calculation used in Gassmann (Figure 38). Also, dynamic and static models (routinely used for field development decisions) will be also affected.

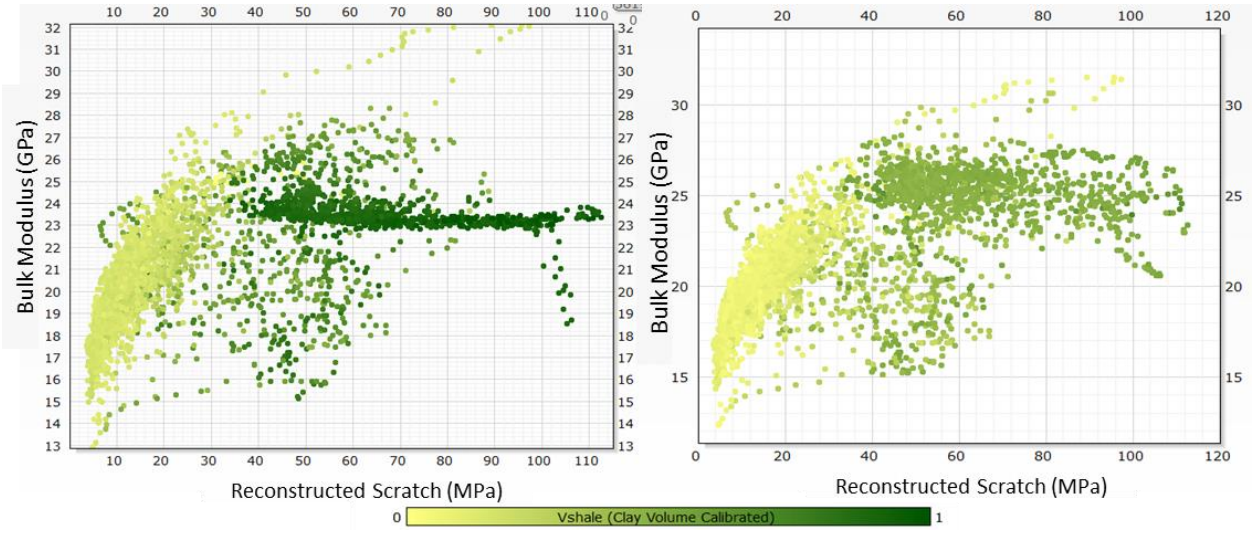

Figure 38. Cross plot between bulk modulus and scratch test showing the difference between a calibrated clay volume and porosity (right) vs uncalibrated (left).

10. Recommendations

As a result of this study, the following recommendations can be made:

Model the overburden, underburden and upper-to-lower Schlochteren differential mechanical response using this study to understand field depletion: As shown in Figure 32, distinctive Cm-porosity trends between sands and the two shales (Ten Boer and Carboniferous) are observed, which in turn begs for testing field depletion scenaria. In the case of Schochteren in particular, the main message is that the upper Scholchteren is more homogeneous than lower Schlochteren (probably due to diagenetical processes, among others) and hence it would be more accurate to have this different character correctly reflected in models.

Minimize sampling bias and improve sample representation: The information from core in the database about Upper Slochteren comprises a very large percentage in the total dataset. However, Lower Slochteren, Ten Boer and Carboniferous suffer from lack of information, especially Carboniferous where measurements are very scarce compared to its thickness.

Include mineralogical composition measurements for ground truthing: Information such as clay volume, through XRD, and porosity where very useful for this study. More information about the other lithologies will be useful for the understanding of the section. XRD sample measurements were very useful determine and calibrate mineral volumes. A continuous log can be acquired by running an electron microscopy tool to investigate the mineral composition continuously. A continuous mineral composition log can have an added value to investigate, as it can reveal information about cement content and clay volume. It has been reported that the Permian section includes anhydrite. However, no XRD samples has recorded anhydrite content, which can cause a bias. Also, mineral composition is valuable for a more accurate estimations of Gassmann fluid substitution and calculating dynamic mechanical properties since this study only assumes clay and sand lithologies.

Use the scratch test as an instrumental core-to-log calibration measurement: Performing more scratch test from the nearby cored wells can be useful as a quick experiment to provide a continuous information to understand and correlate the rock strength across the field. The scratch test is affordable and cheap, with high value-of–information measurement, and we strongly recommend its use for core-to-log integration studies.

Integrate the mechanical-facies model with in-well optical fiber measurements. Potential for differential depletion due to differential mechanical properties should be tested against and corroborated with in-well observations and compaction data collected with optical fiber within the same well.

Consider the depletion stage of the field during data acquisition: Conditions during data acquisition need to be considered. Data acquired through logging was performed in a depletion stage and during a pore pressure of about 10 MPa. Therefore, a consideration to this information when conducting triaxial tests can provide more relevant results.

11. Conclusion

The recently drilled well in the Groningen field was aimed to provide a more in depth understanding of the seismic and subsidence activities. Wide database was built, through many lab tests, to be analyzed to arrive to a better prediction about rocks responses with depletion.

In this study, the analyzed data, continuous and spot, were interpreted and calibrated to be inputted for modeling. Information such as XRD, scratch test, mechanical tests and Hounsfield number were vital for the workflow to achieve more accurate and informative results. Models based on a calibrated electro facies suggest that Slochteren formation split into two sections and have different mechanical and lithological characteristics. Depositional model showed a similar distinction of the Slochteren formation, which can be comparable to the information suggested by the electro facies based model. Also, the shale units of the Ten Boer and Carboniferous are different from each other and distinctive from the other formations lithologically and mechanically.

12. Disclaimer

The core analysis data used in the study are preliminary. Final data, that can be ultimately quoted in further research and literature, will be published in the official NAM platform outside and independently of this report.

13. References

Allen, M. N. & Mayugai, D. R., 1969. SUBSIDENCE IN THE WILMINGTON OIL FIELD, LONG BEACH, CALIFORNIA, U.S.A..

Anon., 1982. Fundamentals of Core Analysis, Core Laboratories Inc. Houston.

Anon., n.d. *Groningen gasfield.* [Online]
Available at: http://www.nlog.nl/en/groningen-gasfield

Archie, G., 1942. The electrical resistivity log as an aid in determining some reservoir characteristics. *Trans AIME,* Volume 146, pp. 54-61.

Ballard, T. & Beare, S., 2016. Particle Size Analysis For Sand Control Analysis. *SPE,* Issue SPE Article: 165119.

Breunese, J. N. & Theinen-Visser, K. V., 2015. Induced seismicity of the Groningen gas field: History and recent developments.

Cantatore, A. & Müller, P., 2011. Introduction to computed tomography.. *Kgs.Lyng by: DTU Mechanical Engineering.*

Cullity, B. D., 1978. *Elements of o X-Ray Diffraction.* 2nd Edition ed. s.l.:Addison-Wesley Publishing Company Inc..

Dagrain, F. & Germay, C., 2006. Field applications for the scratching test. *Proceedings of the ISRM Regional Symposium EUROCK 2006 , Liege, Belgium.*

de Waal, J. A. v. T.-V. K. &. P. J. P., 2015. Rate Type Isotach Compaction of Consolidated Sandstone. *49th US Rock Mechanics/Geomechanics Symposium.*

Den Haan, E., 1994. Vertical compression of soils. *PhD thesis. Delft University of Technology (Delft).*

Epslog, T. L. -., 2018. *Anisotropy of Shale Due to Bedding in Scratch Experiments* [Interview] (17 7 2018).

Ferreira, F. H., Santos, E. R. S., Machado, A. B. & Folador, D. R., 2016. Rock Mechanical Properties Estimation For A 3D Mem: From Logs To Lab. *Rio Oil & Gas Expo and Conference.*

Fjaer, E. et al., 2008. *Petroleum Related Rock Mechanics.* s.l.:Elsevier.

Fleming, R., 2018. *Dutch Government Decides to Cease Gas Production From Groningen Gas Field - A Legal Perspective.* [Online]
Available at: https://energyandclimatelaw.blogspot.com/2018/03/dutch-government-decides-to-end-gas.html
[Accessed 11 7 2018].

Gassmann, F., 1951. *Über die elastizität poröser medien: Vierteljahrss-chrift der Naturforschenden Gesellschaft.* Zurich: s.n.

Gaupp, R., Gast, R. & Forster, C., 2000. Late Permian Playa Lake Deposits of the Southern Permian Basin (Central Europe). *AAPG Studies in Geology,* Volume 46, pp. 75-86.

Gaupp, R. & Okkerman, J. A., 2012. Diagenesis And Reservoir Quality Of Rotliegend Sandstones In The Northern Netherlands—A Review.. *SEPM (Society for Sedimentary Geology),* Issue ISBN 978-1-56576-300-5,, p. p. 193–226..

Gaymard, R. & Poupon, A., 1968. Response Of Neutron And Formation Density Logs In Hydrocarbon Bearing Formations. *The Log Analyst,* Volume 9, pp. 3-12.

Geertsma, J., 1961. Velocity-Log Interpretation: The Effect of Rock Bulk Compressibility. *SPEJ,* pp. 235-248.

Geertsma, J., 1973. Land subsidence above compacting oil and gas reservoirs. *Journal of Petroleum Technology:,* pp. 734-744.

Germay, C. et al., 2015. The Continuous-Scratch Profile: A High-Resolution Strength Log for Geomechanical and Petrophysical Characterization of Rocks. *SPE,* 18(3).

Glennie, K., 1972. Permian Rotliegendes of Northwest Europe Interpreted in Light of IVIodern Desert Sedimentation Studies. *AAPG,* 56(6), pp. 1048-1171.

Hejmanowski, R., 1995. Prediction of surface subsidence due to oil or gasfield development. *5th International Symposium on Land Subsidence FISOLS'95, 16–20 October 1995, The Hague, the Netherlands,* p. 291–300.

Hettema, M. H. H. S. P. M. T. M. V. B. J. M. &. G. H. J., 1996. Production-Induced Compaction of a Sandstone Reservoir: The Strong Influence of Stress Path. *SPE,* 11(2).

Hicks, W. & Berry, J., 1956. Application of Continuous Velocity Logs to Determination of Fluid Saturation of Reservoir Rocks. *Geophysics,* Volume 21, pp. 739-754.

Hill, R., 1952. The elastic behavior of crystalline aggregate. *Proc. Physical Soc,* pp. 349-354.

Hol, S. et al., 2018. Rock Physical Controls on Production-induced Compaction in the Groningen Field. *Scientific Reports.*

Ijasan, O., Torres-Verdín, C. & Preeg, a. W. E., 2013. Interpretation Of Porosity And Fluid Constituents From Well Logs Using An Interactive Neutron-Density Matrix Scale. *SEG,* pp. 143-155.

Jizba, D. & Nur, A., 1990. Static and dynamic moduli of tight gas sandstones and their relation to formation properties. *Gas Research Institute Report.*

Major, C. O., Pirmez, C., Goldberg, D. & Party, L. 1. S., 1998. High-resolution core-log integration techniques: examples from the Ocean Drilling Program. *Geological Society, London, Special Publications,,* Volume 136, pp. 285-295.

McCann, G. D. & Wilts, C. H., 1951. Mathematical Analysis of the Subsidence in the Long Beach-San Pedro Area. *California institute of Technology, Pasadena.*

McPhee, C., Reed, J. & Zubizarreta, I., 2015. *Core Anlaysis: A Best Practice Guide.* 1st ed. s.l.:Elsevier .

Meliksetian, V., 2018. *The Netherlands Can't Afford To Keep Its Natural Gas Promise.* [Online] Available at: http://royaldutchshellgroup.com/category/groningen-earthquakes/ [Accessed 11 7 2018].

NAM, 2013. Wijziging winningsplan Groningen 2013, inclusief technische bijlage Groningen winningsplan 2013.

Nieto, J. A. & Yale, D. P., 1991. Integration of core anddownbole acoustic measurements - Shear and Compressional. *SPWLA, London.*

Ojik, K. et al., 2011. Integrated stratigraphic framework of the Upper Rotliegend II depositional system. *SEPM Special Publication,* Volume 98, pp. 37-48.

Rashed, M. A., Mansour, A. S., Faris, H. & Afify, W., 2014. Factors Affecting the Ultimate Compressive Strength of the Quaternary Calcarenites, North Western Desert, Egypt. *International Journal of Geological and Environmental Engineering,* 8(2), pp. 117-129.

Raymer, L. & Hunt, E., 1980. An Improved Sonic Transit Time-to-Porosity Transform. *SPWLA.*

Reuss, A., 1929. Berechnung der fliessgrenzen von mischkristallen auf grund der plastizitätsbedingung für einkristalle, Zeitschrift für Angewandie Mathermatik und Mechanik. pp. 49-58.

Richard, T., Dagrain, F., Poyol, E. & Detournay, E., 2012. Rock strength determination from scratch tests. *Engineering Geology,* Volume 147-148, pp. 91-100.

Rojas, R., 1996. Neural Networks,. *Springer-Verlag, Berlin.*

Sardar, J.-P., 1993. Use of Porosity as a Strength Indicator for Sand Production Evaluation. *SPE.*

Schutjens, P. M. T. M. d. R. H. v. M. J. G. S. C. M. &. W. J. L., 1996. Production-Induced Compaction of the Brent Field: An Experimental Approach. *SPE,* 11(2).

Schutjens, P. et al., 2004. Compaction-Induced Porosity/Permeability Reduction in Sandstone Reservoirs: Data and Model for Elasticity-Dominated Deformation. *SPE,* 7(3).

Segall, P., 1992. Induced stresses due to fluid extraction from axisymmetric reservoirs. *Pure and Applied Geophysics,* p. 535–560.

Simon, J. B. & Pye, K., 2001. Gradistat: A Grain Size Distribution And Statistics Package For The Analysis Of Unconsolidated Sediments. *Surface Processes and Modern Environments Research Group, Department of Geology, Royal Holloway University of London, Egham, Surrey, TW20 0EX, UK.*

Stauble, A. J. & Milius, G., 1970. Geology of Groningen Gas Field, Netherlands. *AAPG,* pp. 359-369.

Sulak, R., 1991. Ekofisk Field: The First 20 Years. *SPE Journal of Petroleum Technology,* 43(10).

Techlog, 2016. Help Manual.

Thienen-Visser, K. v. & Peter A., F., 2017. The future of subsidence modelling: compaction and subsidence due to gas depletion of the Groningen gas field in the Netherlands. *Netherlands Journal of Geosciences,* pp. 105-116.

TNO, 2., 2013. *Toetsing van de bodemdalingsprognoses en seismische hazard ten gevolge van gaswinning van het Groningen veld, TNO rapport 2013 R11953,* s.l.: TNO.

Uijen, W. M. v., 2013. Rotliegend geology in the Southern Permian Basin: the development of synrift sediments and its relation to seismic imaging. *Department of Earth Sciences, Faculty of Geosciences, Utrecht University, The Netherlands.*

Van Opstal, G., 1974. *The effect of base-rock rigidity on subsidence due to reservoir compaction.* Denver, CO, s.n., p. vol. 2: 1102–1111.

Van Thienen-Visser, K. et al., 2015. Recent developments on the seismicity of the Groningen field in 2015. *TNO.*

Voigt, W., 1889. Über die Beziehung zwischen den beiden Elastizitätskon-stanten isotroper Körper, Wied. pp. 573-587.

Wang, R., Lorenzo-Martin, F. & Roth, F., 2006. a new code for calculating co- and post-seismic deformation, geoid and gravity changes based on the viscoelastic-gravitational dislocation theory. *Computers and Geosciences,* p. 527–541.

Wood, A. W., 1955. A Textbook of Sound. *The MacMillan Co., New York, 360pp..*

Wright, V. P., 1992. Paleosol Recognition: a Guide to Early Diagenesis in Terrestrial Settings. In: *Developments in Sedimentary.* Amsterdam: Elsevier, pp. 47-61.

Wyllie, M., Gregory, A. & Gardner, G., 1956. Elastic Wave Velocity in Heterogenous and Porous Media. *Geophysics,* 21(1), pp. 41-70.

Yale, D., 1993. A comparison of static and dynamic rock mechanical properties. *SEG, Washington D.C..*

Yale, D. & Jamieson, W., 1994. Static and dynamic mechanical properties of carbonates. Issue ISBN 90 5410 380 8, pp. 463-471.

Zhu, X. & McMechan, G. A., 1990. Direct estimation of the bulk modulus of the frame in fluid saturated elastic medium by Biot theory. *60th Ann. Internat. Mtg., Soc. Expl. Geophys., Expanded Abstract,* pp. 787-790..

Zhu, X. & McMechan, G. A., 1990. Direct estimation of the bulk modulus of the frame in fluid saturated elastic medium by Biot theory. *60th Ann. Internat. Mtg., Soc. Expl. Geophys., ,* pp. 787-790.

Zimmerman, R. W., 1990. *Compressibility of Sandstones.* s.l.:Elsevier.

14. Appendix

All samples are ordered with the increase of depth.

Appendix 1a: Routine core analysis with an unstressed condition

number	Grain Density (RCAL)	Permeability (RCAL)	Porosity (Cal-CCl3H)	number	Grain Density (RCAL)	Permeability (RCAL)	Porosity (Cal-CCl3H)	number	Grain Density (RCAL)	Permeability (RCAL)	Porosity (Cal-CCl3H)
	g/cc	mD	v/v		g/cc	mD	v/v		g/cc	mD	v/v
1	2.72	0.09	0.08	154	2.67	120.70	0.20	307	2.66	18.45	0.18
2	2.71	0.01	0.08	155	2.68	88.18	0.20	308	2.66	54.70	0.20
3	2.75	0.01	0.07	156	2.67	99.37	0.23	309	2.68	0.90	0.14
4	2.73	0.01	0.05	157	2.66	288.85	0.26	310	2.66	8.22	0.17
5	2.75	0.01	0.10	158	2.66	47.08	0.20	311	2.66	9.87	0.18
6	2.73	0.01	0.09	159	2.67	154.98	0.23	312	2.66	213.36	0.17
7	2.74	4.65	0.04	160	2.65	453.86	0.27	313	2.67	547.20	0.23
8	2.75			161	2.74	2439.83	0.33	314	2.67	646.74	0.22
9	2.73	0.01	0.11	162	2.68	102.52	0.16	315	2.66	409.01	
10	2.72	0.12	0.05	163	2.68	102.48		316	2.66	171.29	0.18
11	2.68	24.40	0.15	164	2.67	8835.52	0.21	317	2.66	52.45	0.15
12	2.67	370.00	0.23	165	2.65	404.30	0.25	318	2.67	34.36	0.14
13	2.70	26.19	0.15	166	2.69	129.66	0.17	319	2.67	19.88	0.17
14	2.72			167	2.68	63.88		320	2.67	21.72	0.17
15	2.74		0.08	168	2.68	11.72	0.15	321	2.66	20.52	0.23
16	2.83	19.35	0.17	169	2.66	116.10	0.23	322	2.65	162.04	0.15
17	2.70	17.82	0.15	170	2.68	136.77	0.21	323	2.67	14.80	
18	2.72	0.01	0.11	171	2.67	2071.38	0.21	324	2.67	57.97	0.19
19	2.74	0.01	0.10	172	2.67	1086.02	0.15	325	2.70	7.63	0.09
20	2.70	0.01	0.12	173	2.67	91.46	0.20	326	2.67	6.73	0.14
21	2.70	0.04	0.12	174	2.68	59.35	0.20	327	2.66	14.69	0.20
22	2.69	0.09	0.10	175	2.69	101.52	0.18	328	2.67	17.34	0.18
23	2.70	0.06	0.09	176	2.68	160.90	0.23	329	2.66	12.98	0.19
24	2.69	0.01	0.04	177	2.65	214.60	0.13	330	2.73	12.43	0.21
25	2.72	4.44	0.08	178	2.67	325.49	0.25	331	2.67	19.95	0.14
26	2.71	2.13	0.10	179	2.66	233.58		332	2.66	97.10	0.20
27	2.66	7.70	0.16	180	2.58	99.11	0.26	333		491.80	0.26
28	2.76	13.59	0.18	181	2.50	56.54	0.24	334	2.70	4.45	0.12
29	2.66	16.20	0.19	182			0.03	335	2.77	36.26	0.21
30	2.66	16.26	0.19	183	2.68	492.21		336	2.68	24.59	0.18
31	2.66	18.74	0.19	184	2.67	492.21		337	2.66	17.38	0.19
32	2.65	16.21	0.19	185	2.67	61.29	0.25	338	2.66	10.90	0.21
33	2.65	17.36	0.19	186	2.67	89.38	0.23	339	2.66	15.95	0.17
34	2.67	20.48	0.19	187	2.67	142.95	0.22	340	2.66	44.58	0.19
35	2.66	17.59	0.19	188	2.66	212.98	0.19	341	2.67	60.80	0.19
36	2.66	23.14	0.19	189	2.65	211.64	0.27	342	2.72	12.76	

37	2.66	16.55	0.19	190	2.66	75.03	0.28	343	2.72	24.99	0.10
38	2.66	19.03	0.20	191	2.69	28.91	0.28	344	2.67	6.11	0.13
39	2.66	36.20	0.19	192	2.68	152.23	0.17	345	2.68	30.46	0.18
40	2.76	741.21	0.27	193	2.67	275.55	0.30	346	2.69	115.39	0.14
41	2.57	244.47	0.20	194	2.66	398.87	0.28	347	2.67	209.60	
42	2.66	458.85	0.24	195	2.65	502.79	0.25	348	2.65	229.59	0.22
43	2.66	286.44	0.24	196	2.66	427.14	0.28	349	2.66	120.83	0.23
44	2.65	789.05	0.23	197	2.67	270.85	0.28	350	2.70	20.95	0.10
45	2.68	165.66	0.21	198	2.67	263.64	0.33	351	2.71	1.69	0.12
46	2.67	974.12	0.25	199	2.68	267.34	0.29	352	2.71	1.18	0.09
47	2.66	197.89	0.23	200	2.68	201.51	0.31	353	2.71	1.76	0.08
48	2.65	822.29	0.28	201	2.67	165.65		354	2.65	84.34	0.20
49	2.65	677.21	0.28	202	2.68	31.77	0.21	355	2.65	91.10	
50	2.65	467.72		203	2.67	22.96	0.26	356	2.65	85.80	0.21
51	2.65	269.02	0.26	204	2.67	11.17	0.22	357	2.66	45.53	
52	2.65	70.31	0.22	205	2.72	6.73	0.12	358	2.67	5.26	0.16
53	2.66	273.48	0.25	206	2.69	20.75	0.18	359	2.72	95.11	0.20
54	2.66	418.81		207	2.67	20.85	0.22	360	2.66	66.11	0.20
55	2.66	2712.86	0.28	208	2.67	59.49	0.24	361	2.65	87.23	0.22
56	2.66	6296.15	0.27	209	2.79	7.89	0.16	362	2.65	146.39	0.23
57	2.66	370.82	0.25	210	2.68	175.46	0.22	363	2.67	114.87	0.26
58	2.67	360.24		211	2.66	24.63	0.22	364	2.70	27.39	0.15
59	2.67	349.66	0.23	212	2.67	710.29	0.28	365	2.66	12.50	0.17
60	2.66	704.92	0.25	213	2.66	629.75	0.30	366	2.66	4.85	0.13
61	2.65	94.18	0.20	214	2.67	318.26		367	2.66	47.72	0.20
62	2.68	25.37	0.16	215	2.68	23.87	0.20	368	2.64	29.43	0.22
63	2.66	9.24	0.16	216	2.68	13.43	0.19	369	2.67	1.26	0.11
64	2.67	62.24	0.19	217	2.67	34.75	0.20	370	2.65	5.08	0.15
65	2.70	270.16	0.20	218	2.65	326.33	0.27	371	2.68	2.37	0.14
66	2.71	0.72	0.12	219	2.65	359.10	0.27	372			0.24
67				220	2.65	190.30	0.26	373	2.66	88.45	0.21
68	2.68	314.58	0.27	221	2.65	185.64	0.27	374	2.65	30.56	0.16
69	2.67	322.10	0.26	222	2.68	1.13	0.16	375	2.67	7.42	
70	2.67	88.16	0.22	223	2.67	13.28	0.22	376	2.67	1.69	0.12
71	2.66	392.56	0.26	224	2.68	41.45	0.20	377	2.66	2.58	0.12
72	2.66	267.89	0.23	225	2.71	0.36	0.11	378	2.67	4.10	0.12
73	2.67	43.34	0.22	226	2.68	9.80	0.17	379	2.66	37.91	0.14
74	2.64	0.01		227	2.67	34.16	0.20	380	2.65	5.87	0.17
75	2.67	0.01		228	2.69	2.42	0.14	381	2.68	5.20	0.13
76	2.68	0.85		229	2.66	217.66	0.23	382	2.67	29.41	
77	2.70	1.70	0.11	230		189.53		383	2.66	50.70	0.21
78	2.68	1.63	0.15	231	2.67	344.66	0.29	384	2.65	54.11	0.20
79	2.66	54.81	0.22	232	2.66	135.75	0.25	385	2.67	3.91	0.13

80	2.65	342.20	0.26	233	2.66	50.16	0.24	386	2.67	12.01	0.16
81	2.69	22.54	0.14	234	2.67	19.54	0.23	387	2.66	58.79	0.20
82	2.68	22.47	0.19	235	2.67	258.26	0.26	388	2.69	7.77	0.12
83	2.66	37.96		236	2.65	96.12	0.26	389	2.67	4.26	0.16
84	2.66	121.96	0.24	237	2.66	244.15	0.26	390	2.67	2.78	0.15
85	2.68	134.40	0.27	238	2.67	488.19	0.32	391	2.67	7.83	0.15
86	2.71	0.05	0.11	239	2.68	17.16	0.18	392	2.66	4.29	0.15
87	2.68	4.13	0.20	240	2.65	29.12	0.22	393	2.66	4.77	0.15
88	2.66	93.03	0.27	241	2.67	15.37	0.19	394	2.66	15.55	0.18
89	2.67	96.64	0.21	242	2.65	10.01	0.22	395	2.67	29.10	0.19
90	2.67			243	2.64	74.08	0.24	396	2.66	7.71	0.16
91	2.67	85.37	0.25	244	2.65	122.50	0.25	397	2.66	13.49	0.16
92	2.66	64.55	0.23	245	2.65	36.04	0.25	398	2.66	14.22	0.18
93	2.66	5869.07	0.30	246	2.65	180.95	0.27	399	2.66	15.31	0.19
94	2.66	5889.23	0.22	247	2.65	131.10	0.26	400	2.66	63.07	0.18
95	2.68	29.06	0.19	248	2.65	129.69	0.27	401	2.67	60.95	0.19
96	2.66	118.61	0.24	249	2.64	85.96	0.26	402	2.69	17.26	0.20
97	2.68	24.70	0.20	250	2.65	77.57	0.25	403	2.69	26.71	0.19
98	2.68	197.68	0.22	251	2.66	50.28	0.25	404	2.69	19.43	0.12
99	2.65	283.03	0.25	252	2.67	25.81	0.20	405	2.71	3.34	0.12
100	2.68	196.97	0.20	253	2.67	36.29	0.17	406	2.64	45.27	0.17
101	2.65	2354.35	0.29	254	2.66	23.44	0.19	407	2.63	92.19	0.21
102	2.65	136.40	0.24	255	2.66	142.17	0.23	408	2.67	50.19	
103	2.65	386.27	0.27	256	2.66	203.21	0.29	409	2.70	0.45	0.05
104	2.65	101.35		257	2.66	264.24	0.20	410	2.69	1.62	0.14
105	2.67	101.08	0.24	258	2.67	284.71	0.23	411	2.69	5.17	0.14
106	2.68	100.80	0.22	259	2.69	294.53	0.22	412	2.71	1.02	0.12
107	2.69	79.50	0.21	260	2.68	314.15	0.22	413	2.69	3.28	0.14
108	2.67	77.33		261	2.67	349.44	0.22	414	2.65	18.20	0.17
109	2.65	75.16	0.24	262	2.67	428.40	0.25	415	2.69	40.48	0.14
110	2.66	157.94	0.24	263	2.67	452.51	0.20	416	2.68	7.70	0.16
111	2.66	220.22	0.22	264	2.67	417.65	0.22	417	2.68	23.20	0.22
112	2.66	93.26	0.21	265		382.97	0.32	418	2.68	31.22	
113	2.68	17.67	0.16	266		390.17	0.21	419	2.70	2.36	0.13
114	2.65	74.63	0.27	267		297.58		420	2.70	4.74	0.13
115	2.66	141.00	0.23	268		210.59	0.35	421	2.71	6.74	0.21
116	2.70	14.21	0.14	269		123.59		422	2.70	8.05	0.21
117	2.67	111.14		270		36.60	0.20	423	2.68	30.88	
118	2.68	113.85	0.21	271		103.93	0.24	424	2.68	28.11	0.25
119	2.68	110.05	0.16	272		901.36	0.25	425	2.69	2.88	0.20
120	2.69	83.47		273	2.72	880.18	0.17	426	2.74	0.20	0.06
121	2.70	56.90	0.17	274	2.72	223.46	0.23	427	2.68	34.88	0.18
122	2.68	227.05	0.23	275	2.71	341.25	0.11	428	2.67	40.45	0.19

123	2.66	146.54		276	2.73	205.25	0.13	429	2.67	64.53	0.19
124	2.64	66.02	0.20	277	2.74	167.18	0.14	430	2.66	10.20	0.15
125	2.66	183.79	0.22	278	2.73	263.11	0.22	431	2.69	0.40	0.12
126	2.66	485.32	0.23	279	2.73	101.04	0.22	432	2.66	21.52	0.18
127	2.67	536.90		280	2.70	4.94	0.27	433	2.67	13.38	0.16
128	2.67	299.46	0.19	281	2.67	161.72	0.24	434	2.67	18.39	0.20
129	2.67	311.51	0.20	282	2.66	218.17		435	2.67	24.20	
130	2.67	365.87	0.21	283	2.67	355.00	0.24	436	2.67	30.73	0.21
131	2.67	253.38	0.18	284	2.67	483.81	0.25	437	2.68	28.72	0.21
132	2.66	106.29	0.23	285	2.66	395.51	0.20	438	2.72	4.13	0.13
133	2.67	136.36	0.13	286	2.66	280.77	0.19	439	2.68	56.10	0.21
134	2.67	246.16	-0.01	287	2.66	173.96	0.18	440	2.68	16.54	0.19
135	2.65	282.55	0.28	288	2.66	29.00	0.22	441	2.70	0.34	0.11
136	2.66	154.29	0.23	289	2.67	59.59	0.21	442	2.70	189.51	0.13
137	2.67	202.30	0.30	290	2.67	79.94	0.22	443	2.64	11.67	0.17
138	2.69	183.69	0.24	291	2.67	113.85	0.25	444	2.72	0.30	0.09
139	2.69	170.57	0.22	292	2.67	181.91	0.20	445	2.64	622.40	0.18
140	2.66	81.10	0.22	293	2.67	114.67	0.20	446	2.66	8.37	0.20
141	2.66	123.18	0.20	294	2.69	28.89	0.09	447	2.66	8.37	
142	2.65	350.50	0.24	295	2.69	137.93	0.21	448	2.71	22.87	0.10
143	2.69	3.98	0.15	296	2.66	273.79	0.19	449	2.65	9.01	0.19
144	2.66	81.83	0.23	297	2.67	196.98	0.21	450	2.64	21.64	0.19
145	2.69	5.81	0.17	298	2.66	151.04	0.20	451	2.67	5.31	
146	2.66	117.28	0.25	299	2.67	146.63	0.26	452	2.67	4.02	0.12
147	2.67	106.10	0.23	300	2.67	160.03	0.18	453	2.67	2.72	0.16
148	2.67	102.16	0.19	301	2.68	25.94		454	2.68	6.97	0.16
149	2.67	150.99	0.23	302	2.69	146.56	0.10	455	2.67	3.63	0.16
150	2.66	200.04	0.24	303	2.66	94.39	0.20	456	2.67	6.77	0.17
151	2.66	249.42	0.24	304	2.65	29.86		457	2.67	6.23	0.16
152				305	2.65	29.86		458	2.68	3.79	0.15
153	2.69	38.46	0.27	306	2.65	29.86					

Appendix 1b: Routine core analysis with a stressed condition

number	Stressed Porosity	number	Stressed Porosity	number	Stressed Porosity	number	Stressed Porosity
	v/v		v/v		v/v		v/v
1	0.0913	9	0.1579	17	0.198	25	0.1017
2	0.1007	10	0.0846	18	0.1132	26	0.1946
3	0.0974	11	0.2119	19	0.217	27	0.0329
4	0.0986	12	0.2016	20	0.2289	28	0.0469
5	0.1803	13	0.241	21	0.21	29	0.0399
6	0.1752	14	0.2242	22	0.2	30	0.0511
7	0.2226	15	0.1782	23	0.1971	31	0.0471
8	0.2392	16	0.1829	24	0.1059	32	0.0372

Well	Sample No.	Rock Classification	DeOital Components (%)															Authigenic Components (%)																		Porosity (%)				
			Quartz		FSP		Rock Fragments								Accessories			Pore-Filling / Intergranular									Replacive / InOagranular									Point counted				
		Pettijohn (1975)	Monocrystalline quartz	Polycrystalline quartz	Feldspar, unleached	Feldspar, leached/microporous	Chert	Claystone	Claystone, ductile	Sedimentary rock fragment	Metamorphic, indeterminate	Igneous, indeterminate	Rock fragment, indeterminate	Rock fragment, microporous	Muscovite	Heavy minerals (zircon, tourmaline)	Glauconite	Opaque mineral	Quartz	Dolomite/Siderite	Barite	Illite	Chlorite	Kaolinite	Clay, indeterminate/mixed	Grain-rimming clay (mixed)	Grain-rimming (tangential & radial) illite	Grain-Rimming Chlorite	Quartz	Dolomite/Siderite	Feldspar	Opaque/Heavy mineral	Illite	Chlorite	Kaolinite	Clay, indeterminate/mixed	Intergranular	Oversized	Mouldic	InOagranular	SUM Macroporosity
ZRP-3A	P1	Sublitharenite	44.0	9.0	3.3	3.0	0.3	1.3	0	2.7	1.0	1.0	4.7	1.7	0	0	0	0	1.0	0	0.3	0	1.3	1.3	1.7	0	4.3	0	0.3	0	0	0.3	0	0	3.7	0.7	10.7	0	0	2.3	13.0
ZRP-3A	P2	Sublitharenite	40.3	9.3	3.0	2.7	1.0	0	0	1.3	1.0	3.7	4.7	1.3	0	0	0	0	2.0	3.3	0.3	0	0	1.7	3.7	0	3.0	0	2.0	0	0	0	0.7	0	6.7	1.3	3.7	1.3	0	2.0	7.0
ZRP-3A	P3	Sublitharenite	44.3	12.7	2.0	2.0	1.3	0	0.3	0.7	0	1.0	3.3	1.7	0	0	0	0	1.7	0.7	0	0	0.7	0	0.3	0	6.0	6.0	0.7	0.7	0	0.3	0	0	1.3	1.0	7.3	0.7	1.0	2.3	11.3
ZRP-3A	P4	Sublitharenite	38.7	12.0	4.3	4.0	0.7	0	0	1.3	0.3	0.3	6.0	3.3	0	0	0	0	0.3	0	0	0	0.3	0.3	6.0	0.7	2.7	1.3	0	0.3	0	0	0.3	0	4.3	3.3	5.7	1.0	0.7	1.7	9.0
ZRP-3A	P5	Sublitharenite	37.0	16.0	2.3	3.3	0.7	0	0	1.7	0	2.3	3.7	3.7	0	0	0	0	0.3	0	0	0.3	0	2.3	1.0	1.3	4.0	0.7	0.7	0	0	0	0	0	5.7	1.0	10.3	0.3	0	1.3	12.0
ZRP-3A	P6	Sublitharenite	48.0	10.3	1.7	3.7	0.3	0.3	0	1.0	0	1.0	2.7	2.0	0	0	0	0	3.7	0	0.3	0	0.3	0.3	1.0	0.7	5.7	3.3	0.3	0	0	0.3	0	0.3	0.7	1.3	9.0	0	0	1.7	10.7
ZRP-3A	P7	Sublitharenite	46.0	9.0	4.7	2.0	0.7	1.7	0	0.7	0	3.3	3.0	1.7	0	0	0	0.3	0.7	3.0	0.3	0	0	0.7	1.3	0	2.3	0	0.3	0	0	0	0	0	2.0	1.0	13.7	0	0.7	1.0	15.3
ZRP-3A	P8	Sublitharenite	44.7	13.3	1.3	2.3	0.7	0.3	0	0.7	0.3	1.7	3.0	3.0	0	0	0	0	1.0	0.7	0	0.3	0	0.3	3.7	3.7	2.3	0.3	0.3	0	0	0	0	1.0	5.7	1.3	4.7	0.3	1.3	1.7	8.0
ZRP-3A	P9	Sublitharenite	42.0	16.7	4.0	2.0	0.7	1.0	0	0.3	0	3.0	2.7	0.3	0	0	0	0	0	0	0.3	0	0.3	0.3	0	1.7	7.0	4.3	0.3	0	0	0.3	0	0.3	1.0	1.3	7.3	0.3	0.7	1.7	10.0
ZRP-3A	P10	Sublitharenite	50.0	10.7	3.7	4.7	0.3	1.3	0	1.0	0.3	1.0	3.0	2.0	0	0	0	0	0	1.3	0.3	0	0.3	0	2.7	0.7	4.0	0	0.3	0	0	0	0	0	3.3	1.3	5.3	0.3	0.7	1.3	7.7
ZRP-3A	P11	Sublitharenite	43.0	16.3	2.3	2.3	1.7	1.3	0	2.0	0.3	1.7	4.0	0.7	0	0	0	0	0.3	0	0.3	0	0	0	0.7	1.3	5.3	5.3	0	0.3	0	0	0	0	1.0	2.0	5.3	0	1.3	1.0	7.7
ZRP-3A	P12	Sublitharenite	49.7	7.0	3.0	2.3	0.7	1.7	0.7	0	0	1.3	4.0	1.3	0	0.3	0	0	0	5.3	0	1.0	0	0.7	1.7	0.7	5.0	0	0.7	0.3	0	0	0	0.3	1.7	2.0	7.0	0.3	0	1.3	8.7
ZRP-3A	P13	Sublitharenite	44.3	12.0	4.0	3.7	0	1.0	0	0.3	0.3	1.7	1.3	4.0	0	0	0	0	0	0.3	0	0	0	0.7	0	0.7	3.0	0	1.0	0	0	0	0.3	0	2.7	0	16.3	1.0	0	1.3	18.7
ZRP-3A	P14	Sublitharenite	38.7	11.3	1.0	2.7	0.7	0	0	1.3	0	2.3	2.3	3.3	0	0	0	0	0.3	5.3	0	0	0	2.0	6.3	1.0	3.0	0	0	0	0	0	0.3	0	5.7	3.7	5.0	0.7	1.3	1.7	8.7
ZRP-3A	P15	Sublitharenite	50.7	12.7	3.0	1.3	0.3	0.7	0	0.3	0.3	1.3	4.0	3.3	0	0	0	0	0	1.7	0	0	0	0.3	1.0	1.3	6.3	2.0	0.3	0.3	0	0	0	1.3	2.0	0.7	4.0	0	0	0.7	4.7
ZRP-3A	P16	Sublitharenite	42.0	13.0	4.7	3.7	0.3	1.3	0	0.7	0.7	4.7	4.3	1.3	0	0	0	0	1.0	1.3	0	0.3	0	0.3	2.0	1.7	3.0	0	0.7	1.0	0	0	0	0	3.3	1.3	5.7	0.3	0	1.3	7.3
ZRP-3A	P17	Sublitharenite	44.7	10.0	2.0	1.3	0.3	0	0	1.3	0.3	1.7	3.7	0	0	0	0	0	1.0	5.7	0	0	0	0.7	3.7	0.7	1.7	0.3	1.0	0	0.3	0.3	0.3	0.7	5.7	1.7	7.7	0.3	0.3	2.7	11.0
ZRP-3A	P18	Sublitharenite	46.3	15.7	2.7	0	0	0.3	0	0.7	0	1.0	3.3	1.0	0	0	0	0	1.3	0.3	0.7	0	0.3	1.0	9.3	4.3	4.7	0	1.0	0	0.3	0	0	0.3	1.3	1.3	1.7	0	0.7	0.3	2.7
ZRP-3A	P19	Sublitharenite	40.7	12.0	2.0	3.3	2.0	0.7	0	0	0.7	0.7	4.0	2.3	0	0	0	0	0.3	1.3	0.3	0	0.3	0.7	1.3	1.0	4.7	1.0	0.3	0.7	0	0	0.7	0.7	5.0	1.3	11.3	0	0.7	0	12.0
ZRP-3A	P20	Sublitharenite	45.7	9.0	2.3	3.3	0.7	0	2.0	0.3	1.0	1.3	4.3	1.7	0.7	0.3	0	0	1.0	4.7	0	0.7	0.7	0.3	2.3	0.7	2.3	0	0	0	0	0.7	0.3	0	2.3	2.7	7.0	0.7	0.3	0.7	8.7
ZRP-3A	P21	Sublitharenite	38.7	20.3	3.3	0.7	1.0	0	0.3	0.3	0	0.3	2.7	0.3	0	0	0	0	0.3	0.7	0	0	4.3	0	0	1.0	1.3	13.0	0.3	0	0	0	0.3	1.7	2.7	1.3	4.3	0.3	0	0.3	5.0
ZRP-3A	P22	Sublitharenite	40.7	18.0	1.3	1.3	0.7	1.3	0	0.7	0.7	1.0	4.7	1.7	0	0	0	0	2.3	1.7	0	0	4.3	0	1.0	0.7	0.3	4.0	0	0.3	0	0	0	1.7	2.0	0.7	7.0	0.3	0	1.7	9.0
ZRP-3A	P23	Sublitharenite	46.3	14.3	2.7	0	1.0	0.3	1.0	0.3	0	1.0	3.3	1.0	0.3	0	0	0	1.3	2.0	0.3	0.3	2.0	0	3.7	2.7	2.3	1.7	0.7	0	0	0.3	0.7	0.3	2.3	2.0	5.0	0	0	0.7	5.7
ZRP-3A	P24	Sublitharenite	40.0	18.3	2.3	2.3	1.3	0.3	0	0.3	0.3	1.3	4.0	3.3	0	0	0	0	0	3.0	0.3	0	0	1.0	6.0	0.7	0.3	0	0.3	0	0	0	0	0.3	2.7	1.3	9.3	0	0.3	0.3	10.0
ZRP-3A	P25	Sublitharenite	47.7	12.0	3.0	1.7	0	1.0	0.3	0	1.0	0.3	4.0	0.3	0	0	0	0	1.3	5.0	0	0	0.3	0	5.3	2.7	3.0	0	0.7	0	0	0	0	1.0	1.7	2.7	4.7	0.3	0	0	5.0

Appendix 3: Grain Size analysis data

Sample	Kurtosis	Mean Grain Size	Skewness	Sorting	Sample	Kurtosis	Mean Grain Size	Skewness	Sorting
		um					um		
1	7.08544	383.8976636	-1.84648	4.135447	13	10.59447	174.172274	-2.70045	3.151529
2	6.622856	891.0746042	-1.68655	6.790441	14	5.904658	839.2284608	-1.56428	7.231028
3	10.00378	156.7360281	-2.35541	3.010375	15	8.111527	194.2792599	-2.02193	3.472665
4	11.64569	177.0924475	-2.78923	2.968707	16	8.966594	219.4090641	-2.35968	3.541663
5	7.837287	175.2507088	-2.25226	3.670665	17	8.73926	205.5262844	-2.35066	3.54125
6	10.56406	202.1127349	-2.52705	3.345401	18	7.172483	143.7155254	-1.96652	3.545632
7	9.995491	206.849065	-2.35407	3.386294	19	9.829233	158.6336463	-2.33638	2.978532
8	6.896962	1021.758555	-1.8716	7.278188	20	7.961701	184.7767935	-2.21809	3.511344
9	9.359623	173.8866362	-2.3431	3.302191	21	7.17341	151.1479711	-2.19122	3.858016
10	8.148695	154.4845168	-2.27271	3.631026	22	8.054472	171.5627952	-2.33217	3.742429
11	7.891694	168.3891643	-1.82355	3.559567	23	8.656798	193.3576442	-2.44623	3.725974
12	8.711633	139.8700193	-2.26343	3.278799					

Appendix 4a: UCS values from ExxonMobil lab report

Sample	UCS	Sample	UCS
	MPa		MPa
1	53.7	9	9.2
2	29.8	10	2.3
3	45.7	11	8.4
4	28	12	35.4
5	3.2	13	7.6
6	9.6	14	56.6
7	32.7	15	33.2
8	7.4		

Appendix 4b: UCS values from NAM

Sample	UCS	Sample	UCS	Sample	UCS
	MPa		MPa		MPa
1	47.39	4	22.3	7	5.15
2	36.84	5	6.86	8	4.47
3	18.54	6	3.49	9	39.39

Appendix 5a: Averaged elastic parameters from the uniaxial strain experiment by Shell

Sample	Compressibility (Cm)	Young's Modulus (E)	Bulk Modulus (K)	Poisson's Ratio (v)	Sample	Compressibility (Cm)	Young's Modulus (E)	Bulk Modulus (K)	Poisson's Ratio (v)
	1/MPa	GPa	GPa	unitless		1/MPa	GPa	GPa	unitless
1	5.47E-05	14.8	18.28	0.252	9	4.43E-05	18.9	22.57	0.257
2	3.51E-05	19.8	28.49	0.318	10	6.56E-05	12.5	15.24	0.289
3	6.46E-05	14.5	15.48	0.189	11	4.97E-05	16.4	20.12	0.286
4	4.73E-05	18.8	21.14	0.248	12	4.24E-05	17.4	23.58	0.297
5	5.26E-05	16.1	19.01	0.245	13	6.45E-05	15	15.50	0.183
6	5.61E-05	14.5	17.83	0.298	14	5.42E-05	15.3	18.45	0.251
7	5.00E-05	16.7	20.00	0.258	15	4.53E-05	17.3	22.08	0.277
8	7.20E-05	12.7	13.89	0.24					

Appendix 5b: Averaged elastic parameters from triaxial experiment by ExxonMobil

sample	E	v	sample	E	v
	GPa	unitless		GPa	unitless
1	23.50	0.19	7	16.70	0.16
2	18.20	0.19	8	11.76	0.24
3	19.50	0.19	9	7.80	0.30
4	21.47	0.29	10	15.00	0.15
5	10.65	0.21	11	34.78	0.24
6	14.60	0.19	12	27.40	0.21

Appendix 6a: XRD analysis by Shell

Sample	Barite	Dolomite	feldspar	Halite	Hematite	Illite_Mica	K-Feldspar	Kaolinite_Chlorite	phyllosilicate	Plagioclase	Quartz	Siderite
1	0	0.05	0.07	0	0	0.02	0.01	0.04	0.06	0.05	0.82	0
2	0	0.12	0.13	0	0	0.03	0.02	0.04	0.07	0.11	0.68	0
3	0	0	0.19	0	0	0.02	0.04	0.03	0.05	0.15	0.76	0
4	0	0.02	0.17	0	0	0.02	0.14	0.08	0.1	0.03	0.71	0
5	0.01	0.02	0.12	0	0	0.03	0.02	0.06	0.08	0.1	0.77	0
6	0	0.04	0.16	0	0	0.03	0.04	0.06	0.1	0.13	0.7	0
7	0	0	0.17	0	0	0.02	0.04	0.03	0.06	0.13	0.77	0
8	0.01	0.08	0.15	0	0	0.03	0.11	0.08	0.11	0.04	0.65	0
9	0	0	0.14	0	0	0.06	0.03	0.04	0.1	0.11	0.76	0
10	0	0.02	0.15	0	0	0.03	0.03	0.05	0.08	0.12	0.75	0
11	0	0.06	0.19	0	0	0.03	0.04	0.05	0.07	0.15	0.68	0
12	0	0.01	0.16	0	0	0.03	0.12	0.07	0.1	0.03	0.73	0
13	0	0	0.1	0	0	0	0.02	0.01	0.01	0.08	0.89	0
14	0	0.06	0.13	0	0	0.05	0.1	0.05	0.09	0.02	0.72	0
15	0	0.06	0.17	0	0	0.04	0.03	0.05	0.09	0.14	0.68	0
16	0	0	0.11	0.01	0	0.03	0.03	0.07	0.11	0.09	0.77	0
17	0	0	0.08	0.01	0	0.02	0.01	0.06	0.08	0.07	0.83	0
18	0	0.02	0.06	0	0	0.03	0	0.02	0.06	0.06	0.86	0
19	0	0.02	0.07	0	0	0.04	0.06	0.06	0.09	0.01	0.82	0
20	0	0	0.08	0	0	0.04	0.01	0.08	0.12	0.07	0.8	0
21	0	0	0.06	0.01	0	0.03	0	0.05	0.08	0.06	0.84	0.01
22	0	0	0.09	0	0	0	0	0.04	0.05	0.09	0.86	0
23	0	0	0.08	0	0	0.03	0	0.05	0.07	0.07	0.85	0

Sample	Anatase	Barite	Ca_Dolomite	Calcite	Chlorite	Dolomite	Fe_Dolomite	Halite	Hematite	Illite	Illite/Smectite	Jarosite	K-Feldspar	Kaolinite	Mica	Plagioclase	Quartz	Siderite
1					5.1	14		0.4	2.3	16.8	6.4	0.6	3.6	1.1	10	5.3	34.5	
2					4.4		4.1	0.6	1.6	16	6.3	0.4	3.1	1	7.5	6.3	48.5	
3					5.6		2.7	0.6	2.9	29.6	8	0.7	4	1.5	4.2	4.5	35.8	
4	0.7				5.6	1.7		0.3	2.8	34.3	8.6	0.9	4.9	0.9	1.7	3.9	33.7	
5		0.3			0.3	3		0		5.2	1.8		5.4	3	0	8.6	72.2	
6					0.3	2.7				2.4	2.8	0.3	4.1	3.4	0.9	8	75.2	
7					0.5	0.3		0		4.6	1.6		6.2	3.1		9.6	73.9	
8					7.1		2.2	0.8	4.3	38	9.1	1	5	1.6	6.5	3.8	20.6	
9					6.3	2	1.4	0.6	2.4	30.9	6.9	0.9	5.7	1.7	5.8	4.5	30.9	
10					0.7					5.1	1.7	0.3	6.1	1.9		7.1	76.8	
11			1.8		1.3	1.5				5.2	2.5	0.3	6.3	2.2		8.7	69.9	
12					0.7	0.3	0.3	1		5.9	2	0.3	5	3	0.9	8.6	72	
13			3.1		0.8	1.2		0.4		4.3	1.8		6.6	1.9	0	7.7	71.5	0.5
14			0.8		1.2			0.5		5	1.3	0.3	5.7	1.6	0	6.3	76.2	0.3
15			9.2		0.7	13.7				6.7	2.2	0.3	2.6	1.2	0	6.1	57.2	0.3
16			0.8		0.5					6.5	1.9	0.3	2.9	2.6	0	6.6	76.7	0.8
17					0.3			0.6		5.8	2.3	0.3	2.7	2.1	0	5.8	79.7	0.4
18					0.3			0.6		6.1	1.9	0.3	2.3	2.6	0	6	79.3	0.4
19			0.7	0.3	0.4			0.5		6.8	2.1	0.3	2.3	3	0	6.3	76.4	0.8
20				0.3	1.6	2.5	1.1	0.5		6.1	2.5	0.3	1.8	1	0.5	6	75.9	
21				0.3	2.2	4.5	0.3	0.6		5.9	3.4	0.3	1.3	1	0.4	5.9	73.8	
22	0.8				7.7	0.8		0.3	0.3	32	7.4	0.6	3.2	2.8	2.3	7.9	31.4	2.5
23	1.1				7.4	0.8		0.3		25.8	7.3	0.4	2.8	2.2	4.7	8.2	35.7	3.3
24	0.8				7.8	1.2		0		27.8	6.5	0.6	3.3	2.9	2.2	7.6	35.2	4
25			0.3	0.6	5.9					28.9	13	0.5	1.2	5.3	11.1	6.9	23.1	3.2
26	1.5				8.5	0.4		0.3		32.4	7.6	0.5	1.2	4.5	5.4	7.5	30	